University of South Bohemia in České Budějovice
Faculty of Science

Evaluation of negative stains for single particle analysis in electron microscopy

Master thesis

Bc. Eva Sýkorová

Tutor: Ing. Zdenko Gardian, Ph.D.

České Budějovice 2018

Sýkorová, E., Bc., 2018: Evaluation of negative stains for single particle analysis in electron microscopy. Mgr. Thesis, in English. – 50 p., Faculty of Science, University of South Bohemia, České Budějovice, Czech Republic

Annotation

Four negative stains, hafnium chloride and europium, samarium and gadolinium nitrates, were tested in single particle electron microscopy as potential alternatives to uranyl acetate, which is recently being widely restricted for its toxicity. The new stains were applied to a structurally well-described plant photosystem I, visualized by a transmission electron microscope and classified in a single particle analysis. The quality of the stains was evaluated by the obtained resolution and ability to provide reliable structural information.

Key words:

Uranyl acetate, lanthanides, negative staining, single particle analysis, electron microscopy

Affirmation:

I hereby declare that I have worked on my master thesis independently and used only the sources listed in the bibliography.

I hereby declare that, in accordance with Article 47b of Act No. 111/1998 in the valid wording, I agree with the publication of my master thesis, in full in electronic form in publicly accessible part of the STAG database operated by the University of South Bohemia in České Budějovice accessible through its web pages.

Further, I agree to the electronic publication of the comments of my supervisor and thesis opponents and the record of the proceedings and results of the thesis defense in accordance with aforementioned Act No. 111/1998. I also agree to the comparison of the text of my thesis with the Theses.cz thesis database operated by the National Registry of University Theses and a plagiarism detection system.

České Budějovice   ……………………..

 April 17, 2018   Bc. Eva Sýkorová

Acknowledgement:

1 TABLE OF CONTENTS

2 ABBREVIATIONS

ARF	Acute renal failure
ARS	Acute radiation syndrome
CTF	Contrast transfer function
Cyt b$_6$f	Cytochrome b$_6$f
ECHA	European Chemical Agency
EM	Electron microscopy
EuN	Europium nitrate
FSC/FRC	Fourier shell/ring correlation
GdN	Gadolinium nitrate
HfC	Hafnium chloride
LD$_{50}$	Median lethal dose
LHC	Light-harvesting complex
MAP	Maximum a posteriori
ML	Maximum likelihood
NMR	Nuclear magnetic resonance
PDB	Protein data bank
PSI/II	Photosystem I/II
RC	Reaction centre
SEM	Scanning electron microscope
SmN	Samarium nitrate
SSNR	Spectral signal-to-noise ratio
TEM	Transmission electron microscope
UA	Uranyl acetate
βDM	β-D-dodecylmaltoside

3 INTRODUCTION

The term single particle electron microscopy (EM) is used in protein structural sciences with still increasing frequency. Currently, the major advances are made on the field of cryo-EM.[1] However, the standard EM technique is never going to be completely replaced for its robustness, accessibility, and quickness. It would further effectively complement the cryo-EM. Nonetheless, an emerging drawback of the standard EM sample preparation needs to be eliminated to keep the pace. The recently discussed toxicity of a commonly used contrasting agent - uranyl acetate (UA) - and consequently derived law restrictions represent serious limitations to standard EM researchers.

The aim of this study is to evaluate several alternative reagents for the standard single particle EM sample preparation and to compare the results with the traditional UA-based method. The detailed chemistry of UA and the alternative stains along with the principles of EM or the biochemistry of the selected sample macromolecule are described further in this section.

3.1 Methods for protein structure characterization

The knowledge of a protein structure is essential for understanding its function and consequently cell mechanisms. There are several methods for 3D protein structure characterization based either on a purified macromolecule or on a computational structure prediction. Among the exact techniques, the X-ray crystallography, NMR spectroscopy and electron microscopy are most common.[2]

3.1.1 X-ray crystallography

X-ray crystallography has brought the largest contribution to the protein structure knowledge so far.[3,4] According to the PDB database, more than 90 % of its protein structures were solved using this method.[5] Generally, a crystal of the examined protein is exposed to a high energy X-ray beam and a unique diffraction pattern is generated. 3D structure elements can then be mathematically derived from this pattern.[3] The results usually reach atomic resolution.[4] However, the requirement of a high-quality crystal makes this technique inapplicable in the cases when a protein is unable to grow crystals, which is typically the problem of membrane proteins.[2]

3.1.2 NMR spectroscopy

The disadvantage of the crystallization process is eliminated with NMR spectroscopy.[6] The basis of this method is the presence of a spin in specific atom nuclei of which the hydrogen

proton is the simplest example. When an external magnetic field is applied as a pulse of specific frequency, the vector of the magnetic field of the nucleus - the spin state - changes its orientation. This phenomenon is referred to as resonance. A resonance spectrum can be obtained from the used frequencies. Not only the isotope itself influences the resonance frequency, but also the nucleus' environment does.[6] An atomic composition and a 3D structure are possible to reconstruct from the obtained resonance spectrum using complex computations.[6,7] A huge advantage of protein NMR is the ability to label the molecules at specific sites by DNA recombination techniques. On the other hand, the method is not suitable for large protein molecules and a relatively high concentrated solution is required (~1mM).[7] The PDB database includes over 8 % of protein structures solved using NMR spectroscopy.[5]

3.1.3 Electron microscopy

The remaining number of protein structures in the database has been, except for a few cases, characterized by electron microscopy.[5] This number has been expanding recently. The trend is expected to continue in the future, since the advances in the cryo-methods has already increased the resolution of the obtained structures to near-atomic values and has therefore eliminated the technique's major disadvantage.[8,9] In comparison to the other two main protein structure characterizing methods (X-ray crystallography and NMR spectroscopy), the sample demands for single particle EM are the most feasible in the meaning of the lack of protein crystal requirement and low usable concentrations and volumes of a protein solution. On the contrary, the sample preparation for cryo-EM can be extremely difficult. The cryo-EM was not used in this study, its description is therefore not included. Detailed information about this technique is accessible elsewhere.[10,11] The process of sample preparation for the standard single particle EM is described further in this section.

3.2 Principles of electron microscopy

Light and electron microscopes have many features in common. Both devices use a system of lenses to magnify objects too small for the human eye. The primary difference is the type of radiation used. The consequence is the distinct magnification and resolution that can be reached. Here, two definitions are at hand. Firstly, magnification describes the increase of an object's dimension.[12] Secondly, resolution denotes the distance of two objects that are possible to recognize as separate by the device.[12] The two measures are connected, increased magnification does not necessarily increase the resolution, though. For example,

the most common microscopic setup, a human eye, is not able to reach higher resolution than 0.1 mm independently from the magnification of the object.[12]

3.2.1 Resolution

As mentioned above, the maximum resolution of a microscope is connected to the type of radiation. Specifically, it is derived from the radiation wavelength. Hence, electron microscope with the electron beam wavelength about 5×10^{-12} m (at 60 kV) is capable of several-order higher resolution than a light microscope, which is limited by the wavelength of the visible light (4×10^{-7} - 8×10^{-7} m).[12] However, the wavelength is not the only defining aspect. A characteristic common to all types of electromagnetic radiation is the diffraction upon contact with a solid object.[13] A new radiation wave, diffracted on the edge of an object, interferes with the initial wave and the resolution is decreased. At high magnifications, the phenomena of diffraction can be seen as so-called Fresnel fringes, bands parallel to the edge of the object.[12,13] When an image of a pinhole is generated in a microscope, a bright area with decreasing circles around it is seen instead of one sharp point. The circles, termed as Airy discs, distort the real diameter of the imaged pinhole, and confuse the separation when two pinhole images are too close. Therefore, the diffraction limits the resolution.[12,14] An Airy disc radius, measured to the first dark ring, is the determination of the resolving power (r) of a device and can be derived from the **Eq. 1**,[12,14]

$$r = \frac{0.612\,\lambda}{n(\sin \alpha)} \quad (\mathbf{1})$$

where λ is the wavelength of the radiation, n is the refractive index and α is the aperture angle. The constant 0.612 was calculated based on the astronomical self-luminous points (stars). The factor $n(\sin \alpha)$ is denoted as numeric aperture, N.A. Airy discs of a single image and of two differently separated images are shown in **Fig. 1**.
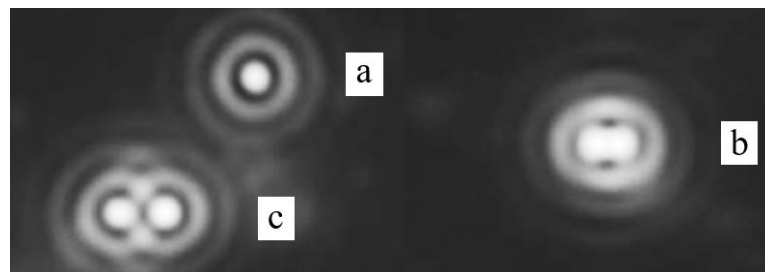

Figure 1. Airy disc (first bright ring) with other decreasing diffraction circles of higher orders shown for a) image of single point object, b) image of a two points with separation under resolution limit, c) image of two points separated by the distance equal to resolution of the microscope. Taken from [14].

3.2.2 Magnification

The magnification (m) of a microscope is expressed as the distance between two points in a final image (d_i) divided by the real distance of the two points in the object (d_o), as is shown in the **Eq. 2**.[12]

$$m = \frac{d_i}{d_o} \qquad (2)$$

Electron microscopes are complex systems of at least three lenses. The total magnification is then calculated as a product of the particular magnifications.[14] It is theoretically possible to magnify an object infinitely. It only brings new information until the resolving power of the microscope is exceeded, though. This useful magnification (m_u) is expressed by **Eq. 3**,[12]

$$m_u = \frac{r_{eye}}{r_{mic}} \qquad (3)$$

where r_{eye} is the resolving power of human eye and r_{mic} is the resolving power for the particular system of lenses. An electron microscope, for example, comfortably reaches the useful magnification of 1,000,000x compared to 1,000x for a precise light microscope.[12]

3.2.3 Electrons in microscopy

So far, the described theory applies to the light as well as electron microscopes. However, there are aspects that make electrons extremely beneficial for microscopy and differentiate it from the optical instruments. The light microscopes evolved for centuries, the development of electron microscopy was possible only after the discovery of the electron's dual wave-particle character, though. De Broglie explained this thesis in 1924 (**Eq. 4**),[12]

$$\lambda = \frac{h}{mv} \qquad (4)$$

where wavelength (λ) was described as inversely proportional to electron mass (m) and velocity (v), h denotes Planck's constant.

From other advantageous electron characteristics, such as low mass or good accessibility, it is the negative charge of the particle that makes it unique for microscopy. The charge allows acceleration and focus of the electron beam by applied voltage and electromagnetic lenses. Moreover, the acceleration voltage (V) influences the microscope resolution, as is expressed in **Eq. 5**,[12]

$$\lambda = \frac{1.23}{\sqrt{V}} \qquad (5)$$

which was derived from a combination of the kinetic energy of a particle, electron charge, applied voltage and de Broglie's expression (**Eq. 4**). A higher accelerating voltage causes shorter electron beam wavelength (**Eq. 5**), thus the resolving power of the microscope is higher (**Eq. 1**).

3.2.4 Aberrations of lenses

Based on this theory, the atomic resolution would be a routine in EM. It is not, though. Microscopists have to deal with lenses' defects and to compromise between sample damage and acceleration voltage. Similarly to optical lenses, the electromagnetic lenses also have spherical and chromatic aberrations.[12,14] Spherical aberration occurs when the electrons passing through a lens further from the vertical axis are focused in a different focal point due to a sharper angle of the diffraction.[14] The chromatic aberration is caused by slightly varying electron energies and consequently divergent effect of the electromagnetic field on their trajectories.[14] While spherical aberration can be successfully eliminated [15], the chromatic aberration is always partially present.[12] Advanced techniques dealing with the main lenses' defects have already achieved the resolution of 1 Å.[16,17]

3.2.5 Types of electron microscopes

Two types of electron microscopes exist. Both are built on the above described principles although their utilization is very distinct. The principal difference is in the type of signal detected.[12] The interaction of an electron with a sample can be elastic, without energy loss, or inelastic, with energy transferred to the surrounding matter.[12,13] Scanning electron microscopes, SEM, take information about the surface of an object from secondary electrons emitted after an inelastic interaction with the primary beam.[12] Transmission electron microscopes, TEM, detect unaffected or elastically scattered electrons after they pass through a specimen and thus serve as an ultrastructure examination tool.[12]

Both electron microscopes consist of one electron source, a system of condenser, projective and objective lenses, a sample chamber and a detector.[12] The source, electron gun, is either a heated cathode (tungsten or lanthanum hexaboride wire), or an emission field gun. The latter uses an electric field to expel the electrons instead of heat.[12] EM uses field of electromagnetic lenses to focus the electrons. The magnetic field is generated by a current flow through a set of copper coils.[12] In addition, numerous other components, e.g. apertures, cameras, extra detectors, cryo-extensions, etc., are present. A very important part of each

electron microscope is a system of vacuum pumps since the use of very light electrons demands operation under ultrahigh vacuum.[12] Simplified schemes of TEM and SEM in comparison to an optical microscope are in **Fig. 2**.
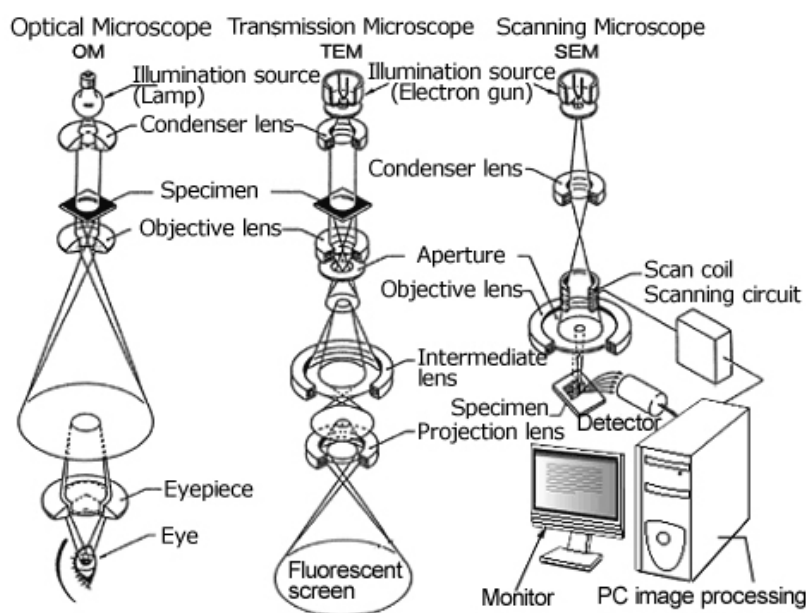

Figure 2. Simplified schemes of a) optical, b) transmission, c) scanning microscopes. Taken from [18].

3.3 Electron microscopy for protein structure recognition

The EM approach in protein structural studies is based on the averaging of a large number of projections of the studied object.[19] Thus, the method consists of two parts, taking images of molecules by a transmission microscope and image processing and mathematical analysis. By averaging thousands of objects (or more), the noise in the image is reduced to the level when a reliable structure visualization is accessible as an electron density map.[19]

Two types of averaging in EM are used. 2D electron crystallography was the firstly developed.[20] Here, 2D crystals of a protein, with the size in the scale of micrometers, are required and the diffraction patterns of these periodic objects are then analyzed. Structures of some of the problematic membrane proteins have been firstly solved by this method, e.g. the light-harvesting complex II (LHCII) from a pea plant.[19,21] Mainly because of the crystal growing difficulty, the second method – random particles averaging – is rather common in recent studies and was also used in our research. This technique, known as single particle analysis, processes large ensembles of randomly oriented single molecules.[19] In comparison with the 2D crystallography, samples of lower concentrations and purities

are needed.[19] The detailed information about single particle processing used in our research is provided in **Section 2**.

3.3.1   Image formation

The image formation in a transmission electron microscope depends on an electron beam scattering after it reaches the sample.[12,13] Generally, electrons encountering heavy atoms exhibit elastic scattering, which changes their trajectories with little or no energy loss. Such electrons are scattered in high angles that disable them to enter the image lenses and thus to contribute to the resulting image. Instead, a dark spot is recorded. This phenomenon forms an amplitude contrast.[12] A partial deflection of electrons is also possible when an inelastic scattering appears. In this case, the electron encountering the sample transfers part of its energy into the surrounding matter while being scattered. However, the angle of the new trajectory is low, and the particle is still able to enter the image. The result of this phase contrast is a light line surrounding an object in the image.[12] With specimens thicker than approximately 60 nm, this type of contrast involves significant chromatic aberration and results in a lower resolution.[12,22]

The biological specimens mostly consist of light atoms (carbon, oxide, hydrogen, nitrogen, sulfur, etc.). Therefore, the amplitude contrast of unstained samples in TEM is minimal.[12] To enhance the contrast, different techniques are used. The most frequent and traditional methods for standard EM sample preparation are positive staining [12,23] followed by negative staining.[12,22] Cryo-techniques deal with the contrast enhancement differently.[22,24]

3.4   Staining in electron microcopy

Both the positive and negative staining techniques are based on the mass density enhancement and thus intensification of the elastic scattering increasing the amplitude contrast.[12] Heavy metal compounds are used for this purpose by both methods. The most common stains are salts of uranium, lead, tungsten, or molybdenum in aqueous or alcoholic solutions.[12]

When positively stained, the metal ions are attached to organelles or macromolecules of the sample which increases their mass and the elastic scattering. These components are then imaged as dark object on a light surrounding.[12,22] Oppositely, the negative stain enhances the density of the surrounding areas and the biological specimens are left uncovered. They are visible as light objects on a dark background in the resulting image.[12,22] Unlike positive, the negative stain is not suitable for ultrathin sections. Instead, it can be successfully used

to increase contrast of compact objects, e.g. cell fractions, macromolecules, or viruses.[12] The stain is able to reveal information about the structure of the object by filling structure gaps and depressions. After the single particle averaging of a large number of the negatively stained objects, the ultrastructure can be solved.[12,22] Huge advantages of negative staining are its relatively low demands on time, equipment, and experience.[12] The principle of negative and positive staining is simplified in **Fig. 3**.

To prepare a negatively stained sample, a supporting layer on the grid is necessary due to the sample particulate characteristic. Standard procedure consists of covering the grid with a plastic film and stabilizing it with carbon.[12] To eliminate potential artifacts implemented by this technique to our comparative study, we purchased pre-coated grids as is described in **Section 2**.
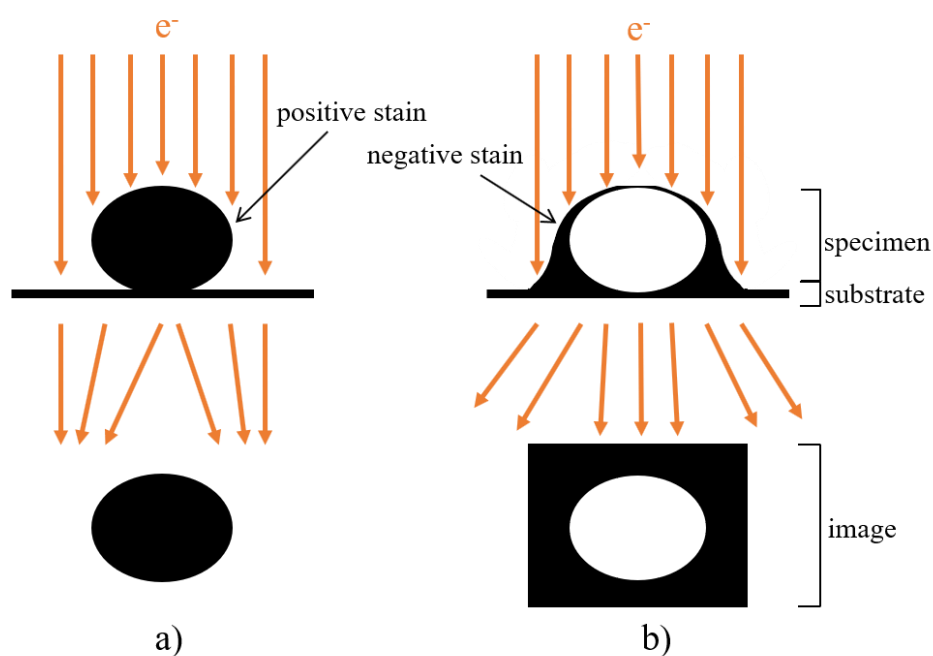
Figure 3. A simplified schema of a) positive and b) negative staining techniques.

3.5 Uranyl acetate

Among the heavy metal salts used for negative staining of macromolecules, uranyl acetate (UA) is the most common. Generally, a 1 or 2% w/v aqueous solution is applied. UA is sensitive to light and precipitates when exposed to phosphate compounds. However, when the storage conditions are well adjusted, the solution is usable for long time periods.[12] Other undesirable effects of UA stain are its reactivity with some of the macromolecule common subunits (phosphate or amino groups) and the relatively low pH (around 4)

of its aqueous solution.[12,22] The first listed allows to use UA also as a positive stain on one hand, but cause artifacts when binding to nucleic or amino acids as a negative stain on the other hand.[12] The second listed makes it impossible to negatively stain particles by UA that are unstable in acidic conditions.[12] In addition, the stain is considerably degraded under high voltage electron beam. This can be effectively eliminated by adjusting the microscope conditions.[12,22] Overall, the advantages such as a simple and rapid application, long solution stability, fine granularity, and strong contrasting effect make UA a logical choice for negative staining of macromolecules, especially for a quick pre-analysis of a specimen.[22] The structural formula of UA is shown in **Fig. 4**.
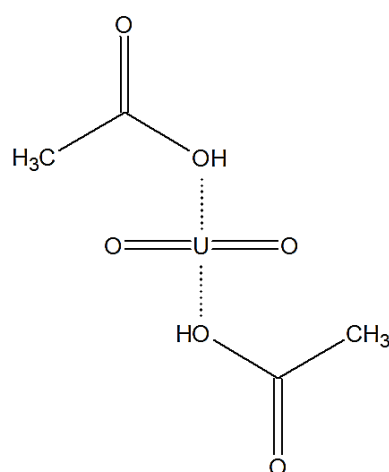

Figure 4. Structural formula of uranyl acetate.[25]

3.5.1 History and properties of uranium

The discovery of uranium is credited to the German scientist M. H. Klaproth, who isolated a dark metallic substance from a Bohemian pitchblende in 1789.[26] 52 years later, H. M. Péligot proved the substance to be uranium dioxide and finally isolated the pure uranium by reducing uranium tetrachloride.[27] However, the radioactive properties of the element remained unknown for another 55 years. It was just the element of uranium, on which the radioactivity was discovered by Henri Becquerel in 1896.[28] In the 20th century, the field of usage of uranium rapidly grew from historical ceramic colouring to military, energetic, medicinal, and scientific purposes.[28]

There are 16 isotopes of uranium of which three are the most abundant on Earth. The most common isotope ^{238}U represents 99,27 % of naturally occurring uranium. The other two are ^{235}U and ^{234}U with 0,720% and 0,006% abundance, respectively.[28] All of the three isotopes are radioactive, emitting α and β radiation. The half-lives of the isotopes range on the scale from 10^5 (^{234}U) to 10^9 years (^{238}U).[28,29] The decay chains of ^{235}U and ^{238}U involve

isotopes of radium and radon among other elements. Both uranium isotopes end as a stable lead ($^{207/206}$Pb).[30] The uranium decay chain is illustrated in **Fig. 5**.

^{235}U is fissile, while ^{238}U is a fissionable material. Fissile elements are able to enter the decay chain with a high probability and even after capturing a low-energy neutron. On the contrary, isotopes that undergo the fission only when induced by high-energy neutrons are referred to as fissionable.[30] Depleted uranium, opposed to enriched uranium, comprises of a lower amount of ^{235}U than its natural abundance and thus is less radioactive.[29] The depleted uranium is nowadays used as a high-density metal in the weapon industry, e.g. for armour plates, or in laboratories for scientific experiments.[29,31,32]

3.5.2 Toxicity of uranyl acetate

There are two types of potential UA adverse effects on living organisms, those caused by its radioactivity and those induced by its chemical toxicity. The radiation health effects of uranium have been studied since the first nuclear bomb was developed.[33] The acute radiation syndrome (ARS) occurs after a short exposure of a high dose of radiation with immediate adverse effects on undifferentiated cells, hematopoietic system, or gastrointestinal system.[33,34] The interest in the long-term health risks also increased with the advanced mining and processing of the uranium.[29] A direct connection between chronical uranium exposure and a lung cancer has been discovered involving radon (^{222}Rn) as a uranium decay intermediate.[31,35] Other possible long-term uranium radiation risks are genetic transformations and birth defects.[31,32,35,36]

The second toxicological view of UA is concerning its chemical reactivity in an organism. Uranium can exist in different oxidation states of which the 6+ and 4+ are the most stable. In the natural environment, uranium occurs mostly as a hexavalent uranyl ion UO_2^{2+}.[29] Certain similarities with chromium ion, which is also stable in 6+ state, indicates the toxicity of UO_2^{2+}.[29] The organs most affected by uranium and similar metals are typically the kidneys. Acute oral or intravenous intoxications result in acute renal failure (ARF).[37,38] Several medical studies have also described acute uranyl poisoning as an inducer of glycosuria, proteinuria, or aminoaciduria.[37,39,40,41] Concrete uranyl metabolism pathways are less known than that of chromium 6+. However, certain adverse reactions have been already described, e.g. ascorbate to dehydroascorbate oxidization [42] or production of hydroxyl radicals.[43] A concerning but perhaps less known effect of uranyl ions is the non-radiative DNA damage. Single strand breaks [29] or oxidative damage on DNA[44] caused by uranium in the presence of activating molecules were described.

Figure 5 — Decay chains of ^{235}U and ^{238}U.

	^{238}Uranium-238 series, includes uranium-234 series						Uranium-235 series			
Np										
U	^{238}U 4.47×10^9 y		^{234}U 2.46×10^5 y				^{235}U 7.04×10^8 y			
Pa		^{234m}Pa 1.16 m						^{231}Pa 3.28×10^4 y		
Th	^{234}Th 24.1 d		^{230}Th 7.54×10^4 y				^{231}Th 25.5 h		^{227}Th 18.7 d	
Ac								^{227}Ac 21.8 y		
Ra			^{226}Ra 1,600 y						^{223}Ra 11.4 d	
Fr								^{223}Fr 22.0 m		
Rn			^{222}Rn 3.82 d						^{219}Rn 3.96 s	
At				^{218}At 1.5 s						^{215}At 1×10^{-4} s
Po			^{218}Po 3.10 m	^{214}Po 1.64×10^{-4} s	^{210}Po 138 d				^{215}Po 17.8×10^{-3} s	^{211}Po 0.5 s
Bi				^{214}Bi 19.9 m	^{210}Bi 5.01 d				^{211}Bi 2.14 m	
Pb			^{214}Pb 26.8 m		^{210}Pb 22.2 y	^{206}Pb stable			^{211}Pb 36.1 m	^{207}Pb stable
Tl				^{210}Tl 1.30 m	^{206}Tl 4.20 m				^{207}Tl 4.77 m	

| = alpha decay; / = beta decay; half-life (d = days; h = hours; m = minutes; s = seconds; y = years)

Figure 5. Decay chains of ^{235}U and ^{238}U.[45]

Uranyl acetate, the most common contrasting agent used in electron microscopy, contains UO_2^{2+} in its molecule. As described above, the uranyl compounds are highly chemically toxic to organisms. The acute LD_{50} (oral intake, mice) is reported as 250 mg/kg.[39] Additionally, even though the substance is made of depleted uranium, UA is recognized as a radioactive material. UA was officially confirmed as a human carcinogen in 2008 at the American Conference of Governmental Industrial Hygienists.[46] Usage of such materials brings other difficulties apart from the danger from intoxication. There are weight limitations for purchase, packaging and shipment restrictions and consequently growing prices. In some countries, e.g. in Japan, the use of UA has been definitely restricted by the government, in others similar laws are being considered.[47,48]

3.6   Alternative stains

Evolving from the UA usage difficulties, many studies searching for effective UA alternatives as a staining agent for TEM have been carried out. Positive results, in the meaning of reaching a comparable contrast to UA, have been described using platinum blue dye [49,50], Oolong tea extract [48,50] or lanthanide salts [47,51], even though none of the new stains proved to be a clearly better staining agent. The majority of the new possible reagents have been tested on ultrathin sections and only several studies concerned single particles, specifically virions, bacteriophages or macromolecular fibrils.[51] Up to date, no data for alternative negative staining of single macromolecules are accessible. In this study, we evaluated lanthanide and hafnium salts as possible staining agents of macromolecules for single particle analysis in comparison with UA.

Hafnium chloride already proved to be an applicable stain for contrasting of sections with plant or fungal cells [52] and was then chosen as an evaluated stain in this study. Acetic salts of gadolinium and samarium were successfully tested even on virions and fibrils.[47,51] These lanthanides, in the form of commonly accessible nitrates, were therefore also selected for the analysis. Another lanthanide compound was added to the list of tested reagents - gadolinium nitrate. The evaluated stains, their formulas and molecular weights are listed in **Tab. 1**.

Table 1. List of tested negative stains, their formulas, and molecular weights.[53]

Heavy atom	Oxidation state	Chemical name	Molecular weight [g/mol]	Molecular formula	Abbreviation
$_{92}U$	6+	Uranyl acetate di-hydrate	424.15	$UO_2(CH_3COO)_2.2H_2O$	UA
$_{72}Hf$	4+	Hafnium chloride	320.29	$HfCl_4$	HfC
$_{64}Gd$	3+	Gadolinium nitrate hexa-hydrate	451.35	$Gd(NO_3)_3.6H_2O$	GdN
$_{63}Eu$	3+	Europium nitrate penta-hydrate	428.05	$Eu(NO_3)_3.5H_2O$	EuN
$_{62}Sm$	3+	Samarium nitrate hexa-hydrate	444.46	$Sm(NO_3)_3.6H_2O$	SmN

3.6.1   Lanthanides

Lanthanides, the fifteen elements of atomic numbers from 57 to 71, are metals found in the f-block, 6th period of the periodic table.[54] Unlike the transition d-block metals, lanthanides have electrons also in the 4f shell, whose energy is lower than that of the 5d. The occupied f orbital causes the effect of lanthanide contraction by the decreasing ability

to shield the nuclear attracting power to the valence shell. The radii of lanthanides thus decrease with growing atomic number.[54] While irregularities occur at atomic radii, the decreasing trend is continuous at +3 ionic radii. For instance, the atomic radii of $_{62}$Sm, $_{63}$Eu and $_{64}$Gd are 1.80, 2.04, and 1.80 Å, respectively. The ionic radii of Sm^{3+}, Eu^{3+} and Gd^{3+} are 1.14, 1.12 and 1.11 Å.[55]

Lanthanides differ from the d-block elements also by their higher reactivity rather similar to the aluminium group of the periodic table. Their preferred oxidation state is generally +3, although some ions naturally occur also in +2 or +4 states, e.g. Sm^{2+}, Eu^{2+}, or Ce^{4+}.[54] Lanthanides react easily with elements of higher electronegativity like F and O. Trihalides LnX_3, exceptionally di- (LnX_2) or tetrahalides (LnX_4), are formed by all lanthanides.[54] Although the field of usability of lanthanides is wide, the quantities consumed are relatively low.[56] The main lanthanide product areas are catalysts, magnets, or glass.[57] In addition, lanthanides can be used as fluorophores in advanced fluorescence-based measuring techniques [58] and they are being tested as potential cancer suppressants.[59] The only lanthanide that exhibit radioactivity is Promethium. The other elements, including Sm, Gd and Eu, are stable with only one or two radioisotopes of low natural abundance and extremely long half-lives.[60] The chemical toxicity of lanthanides and their compounds has not been deeply investigated due to the low consumption. To date, none of the selected lanthanides and its compounds for this study are considered as highly toxic according to European Chemicals Agency (ECHA).[61] The possible health risks stated by the same agency are for example skin, eye, or respiratory irritation.

3.6.2 Hafnium

Hafnium, $_{72}$Hf, is an element of the IV. group of the periodic table ($_{22}$Ti, $_{40}$Zr, $_{72}$Hf, $_{104}$Rf). The preferred oxidation state is +4, although +3 compounds are known.[62] The element is almost identical in its chemical and physical properties to zirconium, $_{40}$Zr. The atomic ($_{40}$Zr 1.45 Å, and $_{72}$Hf, 1.44 Å) or ionic (Zr^{4+}, 0.74 Å, and Hf^{4+}, 0.75 Å) radii are similar due to the effect of lanthanide contraction.[62] Consequently, hafnium is found in zirconium minerals up to a small percent of the mass and the two elements are hardly separable.[62]

Hafnium is highly resistant to hydroxides and acids. Fluoro-complexes are formed under the reaction with hydrofluoric acid.[62] Among boron and cadmium, hafnium is used as a material for control rods in nuclear reactors for its high neutron absorption properties.[28,62] Naturally occurring hafnium consists of six isotopes ($^{174,176-180}$Hf), of which only ^{174}Hf is radioactive. However, its half-life is on the scale of 10^{15} years.[60] Atomic hafnium

16

is not considered as a radioactive nor highly toxic substance according to ECHA.[61] Hafnium chloride behaves as a Lewis acid and is registered as a cause of skin burns and eye damage after exposal by the same agency.[61]

In comparison to UA, the potential use of the selected chemicals as negative stains for TEM would have minor health risks comparable to the use of other common laboratory reagents.

3.7 Sample macromolecule

To reliably compare the effects of different negative stains, an appropriate sample macromolecule has to be chosen. The main parameters are the reliability of its isolation and a precisely solved 3D structure. Photosystem I (PSI), perfectly meeting both demands, was selected for this study. This protein and pigment antenna complex is one of the four driving macromolecules of photosynthesis. Its structure and function are described further in this section.

3.7.1 Photosynthesis

Photosynthesis is an extremely important series of reactions supplying green plants, algae and cyanobacteria with energy and higher organisms with oxygen. It is generally divided into the light and dark phases.[63,64]

The crucial step of the light phase of the oxygenic photosynthetic organisms is the electron transport from a water molecule through a series of protein complexes and electron carriers. The outcome of the light photosynthetic phase is the reduction of NADP to NADPH and the formation of ATP, the energy carrier. The products of the light phase then enter the Calvin cycle and induce the glucose synthesis in the dark phase. The driving fuel of the light reactions is the protonmotive force generated during the electron transportation.[63,64,65]

The light harvesting and electron transfer cascade in green plants and photosynthetic algae take place in chloroplasts. These organelles contain a system of thylakoids in the stroma (inner space) bound in a separate membrane. The thylakoid membrane of green plants is organized into the stacks of grana or lamellae connecting the granal regions. The inner space of thylakoids is called a lumen, the outer a stroma.[63,65] The important photosynthetic complexes are bound in the thylakoid membrane.[65] A simplified schema of a chloroplast is shown in **Fig. 6**.
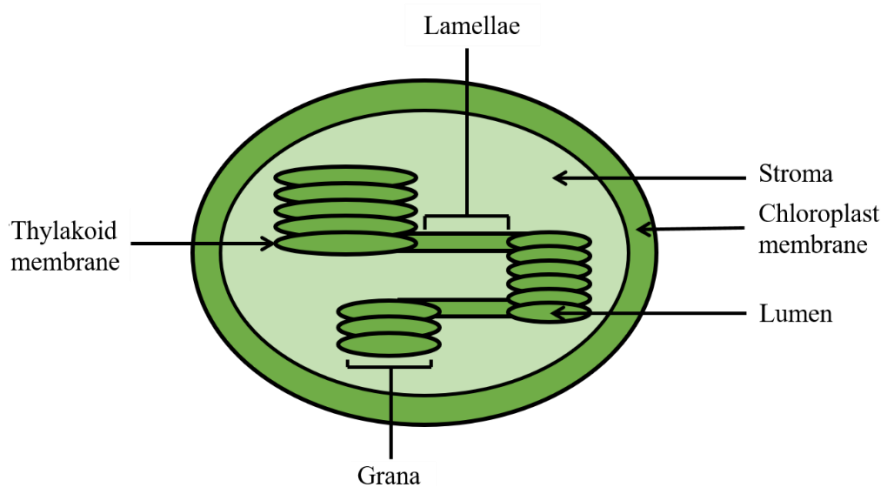
Figure 6. A schema of a green plant chloroplast with the organization of thylakoids into grana and lamellae. Based on [64].

The two main protein complexes mediating the light dependent reactions of photosynthesis are photosystems I and II (PSI and PSII).[64] The PSI and PSII multi-subunit complexes consist of a reaction centre (RC) and a varying number of pigment antennas. The pigment molecules, in plants mainly chlorophylls and carotenoids, absorb a broad range of light and transfer its energy in a cascade to the RC. There, a pair of specialized chlorophyll molecules is excited, and an electron donated by the oxidization of a water molecule is translocated through the thylakoid membrane.[63,64]

Alongside PSI and PSII, cytochrome-b_6f (Cyt b_6f) and ATP synthase are found in the thylakoid membrane.[64] Together they make the four driving proteins of the light phase of the oxygenic photosynthesis. In brief, after a photon absorption, PSII initiates the water oxidation to O_2. Alongside one oxygen molecule, four protons and electrons are extracted. The electrons are further transported through the Cytb_6f to plastocyanine. Subsequently, PSI, driven by the light energy, translocates the electrons from plastocyanine to ferredoxin, from thylakoid lumen to stroma. The ferredoxin then drives the NADPH formation alongside with other regulatory reactions. An electrochemical potential is generated as the electrons are transferred through the thylakoid membrane and it is used as a fuel to the ATP synthase.[64,66,67] A simplified schema of the photosynthetic light phase reactions is shown in **Fig. 7**.

Each of the four main photosynthetic complexes has a different specific location in the thylakoid membrane. While PSII are found mostly in the granal membranes, PSI are typically located on lamellae, as are the ATP synthases. Thy Cyt b_6f molecules sit on the interface between these two regions.[64,65]
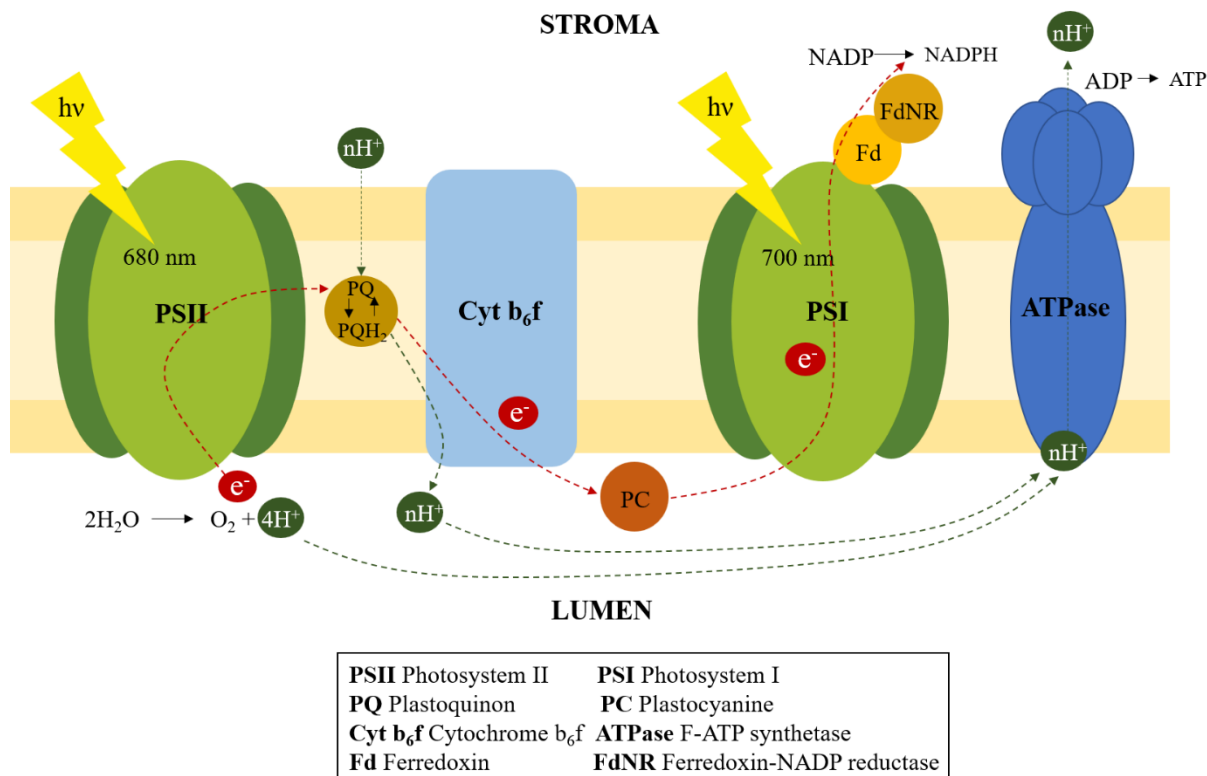
Figure 7. Simplified photosynthetic light phase reactions and the main protein complexes shown in a thylakoid membrane. Based on [64].

3.7.2 Photosystem I

The mechanisms of the photosynthetic light phase reactions were described based on the discoveries of the two functional systems in the 1960s.[68] Firstly, the existence of PSI was described (as the nomenclature refers) although PSII is the first element of the reactions.[69] PSI in green plants is composed of a reaction centre and a light harvesting antenna complex (LHCI).[64,65] The reaction centre is a protein complex including up to 14 individual subunits of which PsaA and PsaB are the most significant. These two proteins bind two chlorophyll molecules located in the middle of the reaction centre. The special pair of chlorophyll pigments, called P700, is excited upon the absorption of a photon of a specific wavelength (700 nm) and induces the electron transport.[64,65] Beside P700, the PsaA-PsaB heterodimer includes the primary electron acceptors A_0 (chlorophyll a), A_1 (phyloquinon), Fx (Fe_4-S_4 cluster), and other chlorophyll molecules that function as an inner antenna.[65,70] PsaC subunit, for example, binds the terminal electron acceptors of PSI, F_A and F_B (other Fe_4-S_4 clusters). Other Psa protein subunits contribute to ferredoxin, plastocyanin or LHCI binding.[65,70] The green plant and cyanobacterial PSI reaction centres are highly consistent, although there are no extrinsic antennas bonded to the cyanobacterial system.[65,70]

19

The peripheral antenna of plant PSI, LHCI, comprises four subunits.[64] Each subunit is a complex of one protein (Lhca1 – 4) and associated chlorophyll molecules. The whole PSI-LHCI complex contain approximately 200 pigments molecules.[70] The four LHCI subunits arranged into two dimers bind the reaction centre unit and form a half-circle around PSI.[64] The structure of LHCI docked with PSI reaction centre is in **Fig. 8**. The plant unique LHCI adds a significant mass to the PSI molecule (150 kDa of the overall 525 kDa).[70]
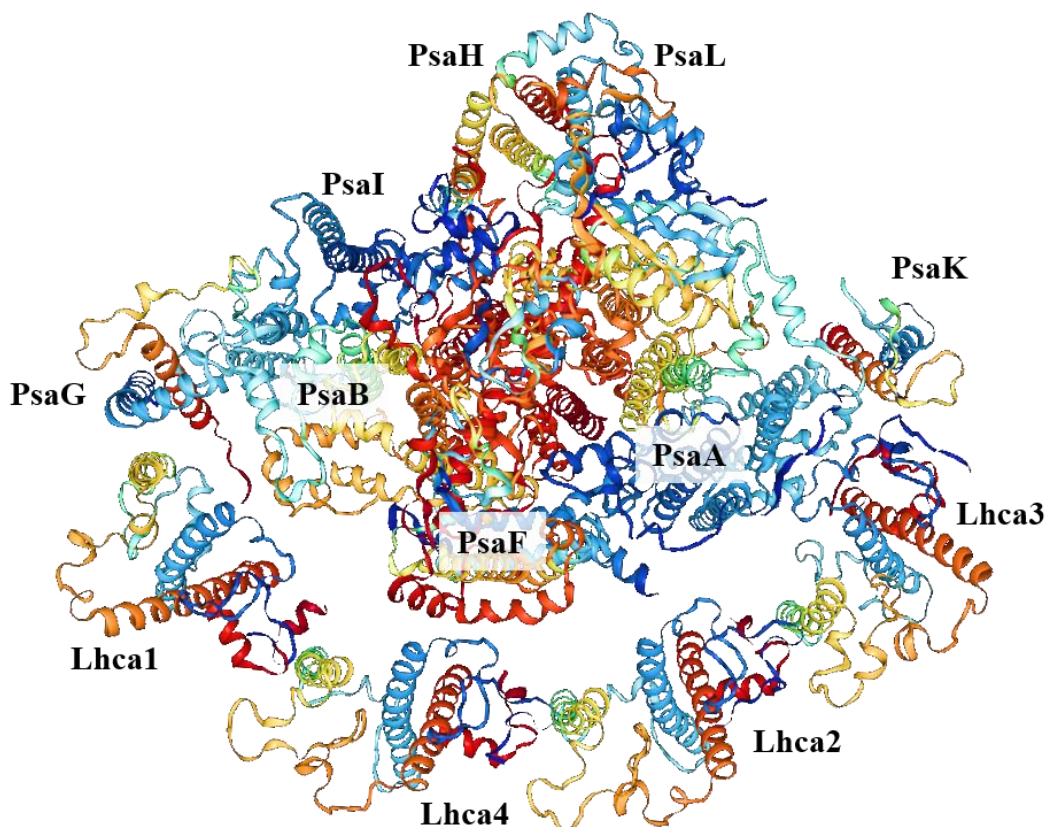

Figure 8. Structure of PSI LHCI and reaction centre, stromal view. Taken from [71].

The 3D structure of plant PSI-LHCI complex has been credibly solved by X-ray crystallography, recently reaching the resolution of 2.6 Å.[71] PSI-LHCI was also among first single molecules studied by single particle electron microscopy.[72,73] Recently, EM studies on algae or bacterial PSI have been carried out.[74,75]

4 MATERIAL AND METHODS

4.1 Isolation

PSI-LHCI complexes were isolated from the leaves of a pea plant (*Pisum sativum*) grown in a standard laboratory conditions for 21 days. Firstly, the whole fragments of thylakoid membranes with the photosynthetic macromolecules still incorporated were purified. The procedure involved homogenization of the freshly harvested leaves in a grinding buffer (50mM KH_2PO_4, 350mM KCl, 0.5 mM NaEDTA, pH 7.5), solubilizing the centrifuged pellet in a tricine-sucrose buffer (50mM tricine, 200mM sucrose, 100mM NaCl, 5mM $MgCl_2$, pH 8.0) and again homogenizing the new pellet in a MES-buffer (2mM MES, 15mM NaCl, 5mM $MgCl_2$, pH 6.3). In this phase, the membrane-bound macromolecules are able to endure low temperatures (-70 °C) and thus can be stored for further processing. This part of isolation was therefore done only once.

In the next step, the purified thylakoid fragments were solubilized by β-D-dodecylmaltoside (βDM, 1.5% w/w concentration in the final solution). The solubilizing agent degraded the thylakoid membrane and released the individual photosynthetic macromolecules to the solution (PSI, PSII, ATPase and others). The structural formula of βDM is in **Fig. 9**.
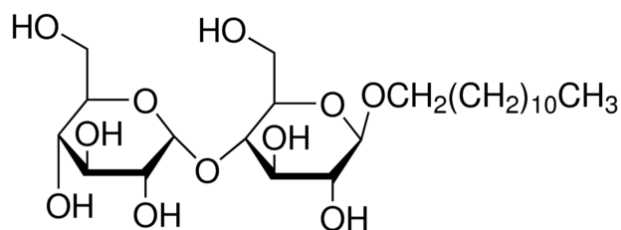

Figure 9. Structural formula of β-D-dodecylmaltoside, the non-ionic surfactant used in this study for thylakoid membrane solubilization. Taken from [76].

The macromolecular complexes were then separated in a continuous sucrose gradient. The principle of this method is the sedimentation of molecules in an increasing sucrose density due to their size, mass and centrifugation force. It is a common method for separation of DNA, RNA and protein molecules and is extensively used in photosynthetic studies.[77] The continuous sucrose density gradient was achieved by a slow defrosting of the centrifuge tubes that were previously filled with the solution of sucrose in the MES-buffer (0.55M concentration with 0.02% w/w βDM) and put into -70°C for approximately one hour. In general, the sucrose defrosts at a lower temperature than pure water, concentrates

on the bottom of a centrifuge tube due to its high density and the continuous gradient is formed. The βDM solubilized samples were then carefully layered on the top of the gradient and the tubes were centrifuged (ultracentrifuge, high vacuum, 4°C, 17 hours, 36,000 rpm, SW 41 Ti Swinging Bucket rotor, Beckman). The discrete layers, each representing a different type of molecules, were then carefully transferred into separate microtubes.

The steps of βDM solubilization and sucrose gradient separation were performed each time before microscopy imaging due to a time degradation of the solubilized PSI-LHCI macromolecule. The above described process of PSI-LHCI isolation was derived from previously described purification methods, e.g. in [78] or [79].

4.2 Sample identification

Two methods were used to characterize the isolated macromolecules, an electrophoresis, and fluorescence spectra analysis.

4.2.1 Electrophoresis

The electrophoresis was performed with a NuPAGE Electrophoresis® System (Thermo Scientific) on an acrylamide gel using NuPage reducing agent (dithiothreitol, Thermo Scientific) for a protein solubilization and a PageRuler™ Unstained Protein Ladder (10 – 200 kDa, Thermo Scientific) as a marker. A standard Coomassie blue (Thermo Scientific) staining protocol was used for the gel visualization.

4.2.2 Fluorescence analysis

The fluorescence emission spectra were obtained by a SPEX FLOUROLOG 1681 spectrometer (HORIBA Scientific) with 435 nm excitation wavelength. The samples were measured at liquid nitrogen temperature (77 K, -196.15 °C). Photosynthetic complexes are effectively studied at this temperature when almost all photosynthetic reactions are inhibited. This method is then capable to reliably determine the presence of complex photosystems or separate light-harvesting antennas.[80]

Based on the results (see **Section 5**), the zone of the sucrose gradient containing the separated PSI-LHCI molecules was taken as a sample solution for the microscopy visualization.

4.3 Sample preparation

4.3.1 Sample application

All samples were applied on prefabricated copper grids covered by a carbon layer (400 mesh Cu, Agar Scientific). These grids were put into a glow discharge before sampling to make their surface hydrophilic. The sample concentration was adjusted to an ideal distribution of the protein on a grid instantly before each experiment. The macromolecules on a grid should not be aggregated on one hand nor extremely separated on the other hand. Typically, low concentrations around 0.01 mg/ml are adequate for negative staining techniques. The application itself consists of placing a droplet (5 µl) of sample solution on a grid for a specific time interval before drying it. Macromolecules are being adsorbed on the carbon layer on the grid during the drop exposal. The time interval was again adjusted to the sample distribution and generally varied from 10 to 30 s in this study.

4.3.2 Negative staining

The next step was the negative staining of the samples. The chemicals were purchased in a solid (powder) state (purity > 99 %, Hf and lanthanide salts from Sigma-Aldrich, UA from Electron Microscopy Sciences). Stock aqueous solutions of the selected hafnium and lanthanide salts and of the reference UA were prepared according to **Tab. 2**. The concentration of 2 % w/w was chosen as a standard value for UA single particle negative staining. The same concentration was also used in a lanthanide stains study.[47] The two additional SmN stain solutions of 1 and 3 % w/w concentrations were prepared for a referential analysis of the concentration influence on the staining effect. The staining solutions were prepared once and stored in dark at 4°C for further use except for HfC, which exhibited instability in time and was thus prepared fresh before each staining.

The staining procedure was similar to the sample application (a drop of the particular solution applied on a grid for a specific time interval and then dried). We defined the staining time interval as 10 s for all samples.

Table 2. List of negative stains' aqueous stock solutions and their concentration, volume, and pH.

Stain name	Abbreviation	Stock solution concentration [% w/w]	Stock solution volume [μl]	~pH
Uranyl acetate di-hydrate	UA	2		2.5
Hafnium chloride	HfC	2		1.0
Gadolinium nitrate hexa-hydrate	GdN	2		4.0
Europium nitrate penta-hydrate	EuN	2	100	5.0
Samarium nitrate hexa-hydrate	$SmN_{1\%}$	1		
	$SmN_{2\%}$	2		3.5
	$SmN_{3\%}$	3		

4.4 Visualization

All pictures were acquired by the transmission electron microscope JEOL 2100F with 200 kV acceleration voltage equipped with the Gatan Orius SC1000 CCD camera and a high-resolution pole piece with point resolution guaranteed as 0.23 nm. The samples were viewed at 20,000x magnification with resulting pixel size of 3.4 nm. Several sets of samples were imaged in this study. Firstly, the micrographs of samples stained with different 2% w/w solutions were acquired with > 24h delay from the grid preparations. Secondly, the same set was acquired with no delay from the preparations. Thirdly, samples stained with 1 and 3% w/w solution of SmN were recorded. The effects of the alternative stains were then analyzed by the single particle analysis together with the above described different conditions of micrograph acquisitions.

4.5 Single particle analysis

4.5.1 RELION

All procedures involved in the single particle analysis were completed in RELION. It is an open-source program developed in the MRC Laboratory of Molecular Biology by the research group of Sjors Scheres.[81]

RELION, standing for REgularized LIkelihood OptimalizatioN, uses a Bayesian approach of data extraction for single-particle structure refinement. In brief, the Bayesian data interpretation innovatively deal with the problem of overfitting.[81] It was difficult to detect whether the reconstruction was derived from the real data or from a noise in previously used reconstruction methods. EM single particles are especially prone to overfitting

due to incomplete data (part of information lost during the experiment, e.g. relative orientations of macromolecules) and a high noise (the noise is of even more significant in cryo-EM). An example of pre-Bayesian approach is the upgrade of experimental data by a complementation with prior information, e.g. the smoothness (the scattering potential of macromolecules varies smoothly in space because of chemical bonds).[81] However, this type of reconstruction is to some extent based on arbitrary input and hence can lead to subjectivity and overfitting. Statistical methods utilizing only single function instead of many averaging and filtering processes may reduce the number of arbitrary decisions in the reconstruction. E.g., methods based on the maximum likelihood (ML) estimation finding the most probably correct model of the observed data may be efficient.[82] They are applicable only on large data sets, though. With typically small data sets obtained by EM, the arbitrary inputs are also necessary.[81] Finally, the Bayesian model regulates the ML function by imposing prior distributions on the actual parameters. The posterior distribution is then optimized. This approach is referred to as maximum a posteriori (MAP) estimation.[81] Sjors Scheres used Gaussian distribution on the Fourier components of the signal as a prior estimation in combination with MAP estimation. This Bayesian model serves as a reliable method for single-particle reconstruction with the minimum of arbitrary approach. Although this statistical model has been known for a relatively long time [83], it was firstly applied for EM single particle structure refinement in RELION.[81]

A simplified explanation of the RELION structure reconstruction function as presented by Sjors Scheres [81] is visualized in **Fig. 10**. In the first step of the procedure termed as "Alignment", the information about relative image orientations is derived from the comparison of computer-generated and experimental images in the form of probability distributions over all assignments, not as an optimal orientation for each image.[81] The power of the noise influences the distributions' sharpness. The second step, "Smooth reconstruction", combines the prior data and experimental images into a reconstructed image. The results are then iterated again, typically until no changes in the new structures are observed.[81] The Bayes' law defines the contributions of the experimental and prior data to the result, which is influenced by the powers of noise and signal in the images. The exact calculations and the detailed theory is accessible in [81].
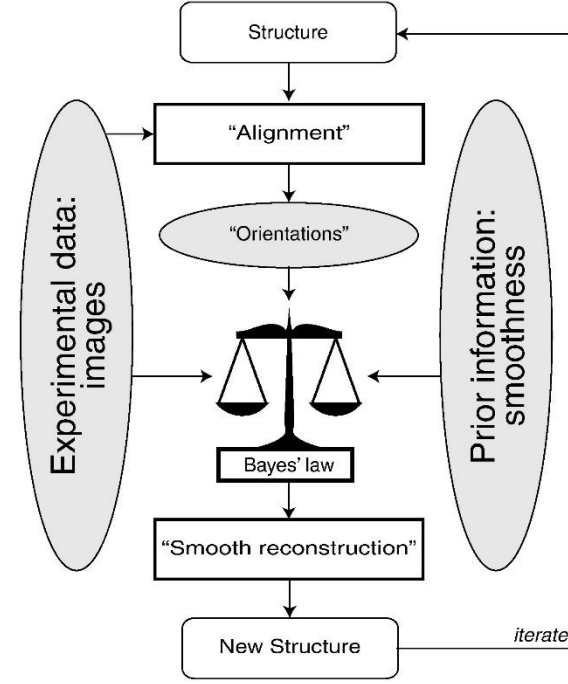
Figure 10. A simplified schema of the RELION structure reconstruction method.[81]

4.5.2 Resolution estimation in RELION

Resolution is a suitable measure to compare the quality of the obtained structure. A gold-standard refinement approach [84,85], used by RELION, enable a reliable resolution derivation. The approach divides the experimental data into two halves (usually as images with odd and even numbers). The refinement and structure reconstruction are made on both halves independently. The resolution of the obtained structure is then accessible from a Fourier shell correlation (FSC) between the two data sets in the case of 3D and Fourier ring correlation (FRC) for 2D reconstructions. Although the terms are historically different, the principle of the correlation function is similar.[86] The independently refined 3D/2D data sets are compared in a 1D function of spatial frequency.[86] The FSC function is expressed by **Eq. 6,**[86]

$$FSC(u,v;s) = \frac{\displaystyle\sum_{||\mathbf{s}_k|-s|\leq\varepsilon}^{k_s} U(\mathbf{s}_k)V^*(\mathbf{s}_k)}{\left\{\left(\displaystyle\sum_{||\mathbf{s}_k|-s|\leq\varepsilon}^{k_s} |U(\mathbf{s}_k)|^2\right)\left(\displaystyle\sum_{||\mathbf{s}_k|-s|\leq\varepsilon}^{k_r} |V(\mathbf{s}_k)|^2\right)\right\}^{1/2}} \quad (6)$$

where U and V are the two Fourier components, s is the magnitude of spatial frequency ($s=|\mathbf{s}_k|$), k is the number of Fourier voxels (pixels in 2D) in the shell (ring) and ε is the selected shell (ring) thickness. The resulting values of the function are correlation coefficients between two Fourier transformed volumes/images over equal shells/rings in the Fourier space.[86]

The threshold FSC (FRC) value at which the interpretable resolution is calculated, is a discussed topic. The FSC (FRC) function is directly related to the spectral signal-to-noise ratio (SSNR), which helps to determine the right threshold. SSNR is expressed as the power of the signal F divided by the power of the noise σ (**Eq. 7**).[86] Its relation to FSC (FRC) calculated from two halves of the data set is expressed in **Eq. 8**.[86]

$$SSNR = \frac{|F|^2}{\sigma^2} \qquad (7)$$

$$FSC(FRC) = \frac{SSNR}{SSNR+2} \qquad (8)$$

The 3σ criterion represents a cut-off for the resolution value, at which no signal was included in the results (SSNR -> 0, FSC/FRC = 0).[86,87] Other criterions determine the value as a point where noise outweights the signal (SSNR = 1, FSC/FRC = 0.33) or as an exact half of the scale (SSNR = 2, FSC = 0.5).[86] The 0.5 threshold has been widely used as a standard value. However, factors as particle symmetry or number of voxels/pixels in a Fourier shell/ring were found to influence the correlation function and should be taken into account.[88] RELION uses the threshold value of 0.143 [84], which was adopted from [89]. An example of FSC curve with a calculated resolution using the 0.143 cut-off is in **Fig. 11**.
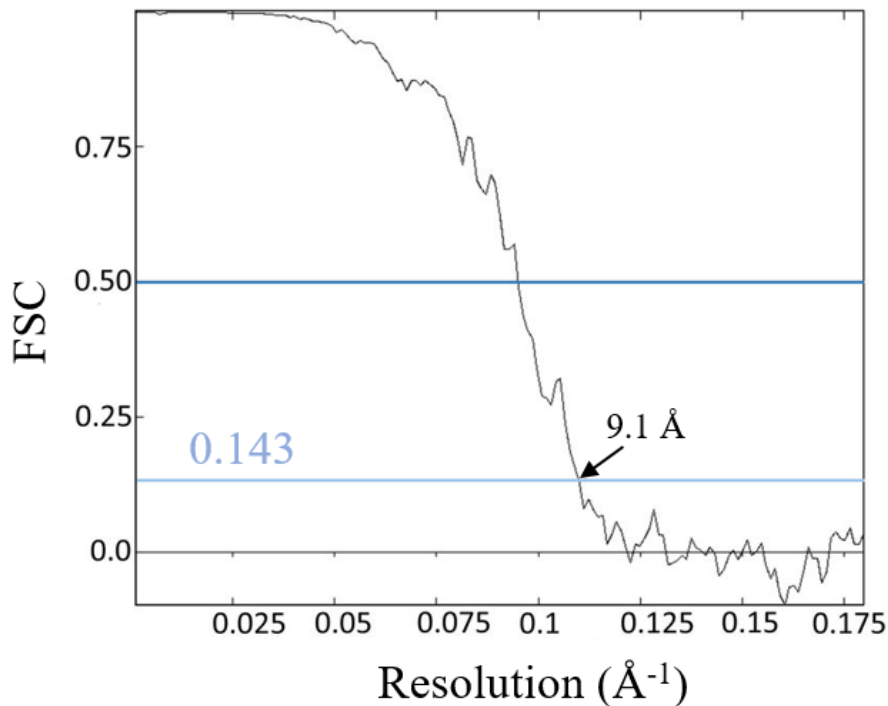

Figure 11. An example of a FSC curve calculated from two independently reconstructed halves of cryo-EM data set (immature Zika virus). The resolution of 9.1 Å was derived at a threshold value 0.143. Taken from [90].

In addition, the final resolution is dependent on the number of particles aligned in the resulting image. The dependence was described as logarithmic.[89,91] In general, more aligned particles lead to a higher resolution until a limit of the particular method is reached. When comparing the resolutions of differently processed samples, variously negatively stained in the case of this study, the number of aligned particles of each of the evaluated images should ideally be similar.

4.5.3 RELION workflow

The practical workflow of a single particle analysis in RELION starts with pre-processing of micrographs, e.g. contrast transfer function (CTF) correction. CTF is a mathematical description of the image modification caused by microscope aberrations and is directly accessed from an image diffraction pattern.[92] The next step is an automatic or manual particle selection and their extraction from the imported micrographs. Again, the extracted particles can be further processed by filtration (e.g. by particle diameter), masking (mask application can lower background of spherical particles), etc. Then, the 2D class averaging is done. The particles are sorted into a number of classes. Many iterations are usually needed to reach a stable result. The process of 2D classification and resolution estimation is similar to that of 3D structure refinement described previously, although the calculations include only 2D data. For the purposes of a structure identification, especially when visualized by cryo-EM, further 3D structure refinement, classification and reconstruction is available in RELION.[93] However, 2D classification is a sufficient method for the evaluation of negative stains' efficiency and the 3D reconstruction was not performed in this study. The process of RELION single particle analysis performed in this study is visualized in **Fig. 12**.
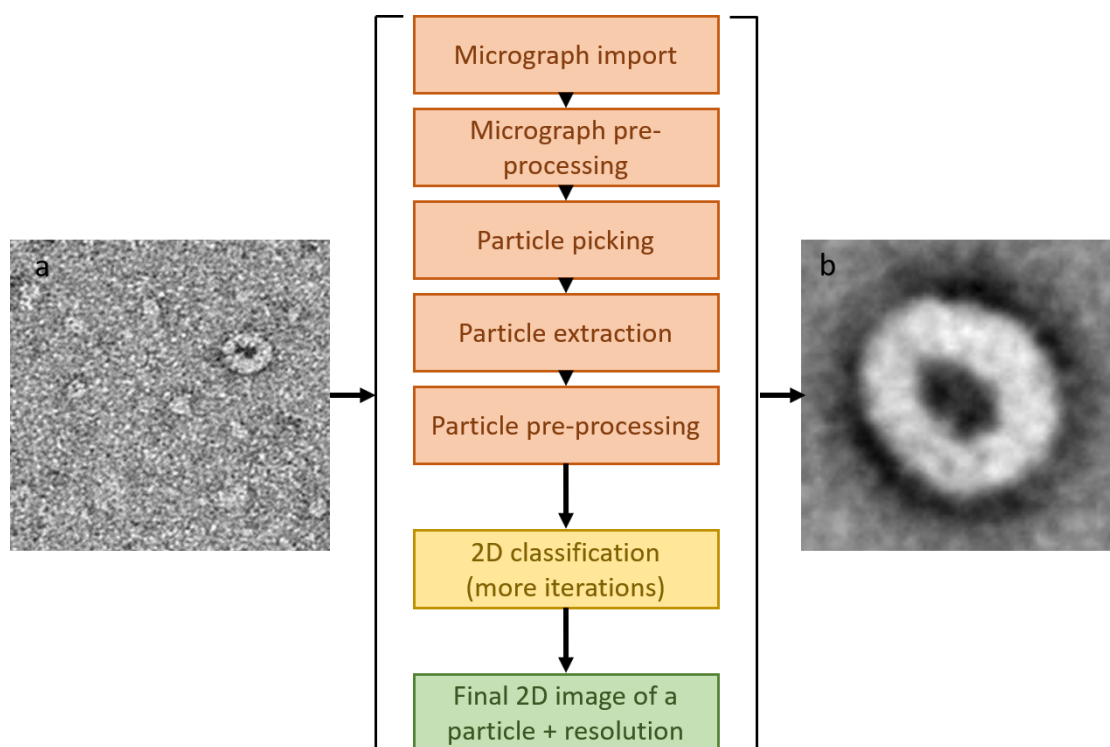
Figure 12. A schematic illustration of a RELION single particle 2D classification workflow with an example of a) unprocessed micrograph and b) one of the final refined particle classes (fucoxanthin-chlorophyll proteins from *C. meneghiniana*). The examples were taken from [94].

4.6 Data evaluation

The resulted images were evaluated by two factors: the obtained resolution and the ability to provide a real structural information. This ability was assessed in the form of grayscale profiles of the 2D classified particles. Generally, a grayscale profile transforms a single line of a determined direction and length in a micrograph into a function of a distance and grey intensity. In the field of single particle analysis, such profile yields information about the distribution of the contrasting agent on the surface of the particle. A higher intensity value means a lighter shade in the image and thus a lower amount of the negative stain on the surface. Ideally, the stain molecules fill the structure gaps of the particle and leave the above areas uncovered so the surface structure can be reconstructed. In such cases, a side-view on the particle 3D model in the right angle should fit into its grayscale profile. In this study, the grayscale profiles of the alternatively-stained particles were compared to the profile of an UA-stained particle as a reference (see **Section 5**). The graphs of the grey intensity of each particle in a specific distance and direction were constructed in ImageJ (freeware, version 1.51j8).[95]

5 RESULTS

5.1 PSI-LHCI isolation

We separated the photosynthetic proteins of solubilized thylakoid membranes in a sucrose gradient (see **Section 4**). Six clearly separated zones (Z1-Z6) were present in the gradient tubes. Monomeric PSI-LHCI complexes were presumably isolated in the zone 4, according to referential studies.[96,97] Particles with higher density, e.g. PSII and antenna complexes or thylakoid membrane fragments, can be found closer to the bottom of the gradient tube where the density of sucrose is rather similar. On the contrary, light pigment molecules or separate LHC antennas are located in the low-density sucrose areas closer to the top. A photograph of the tube with the sucrose gradient with designated six separate zones and their assumed identification is in **Fig. 13**.
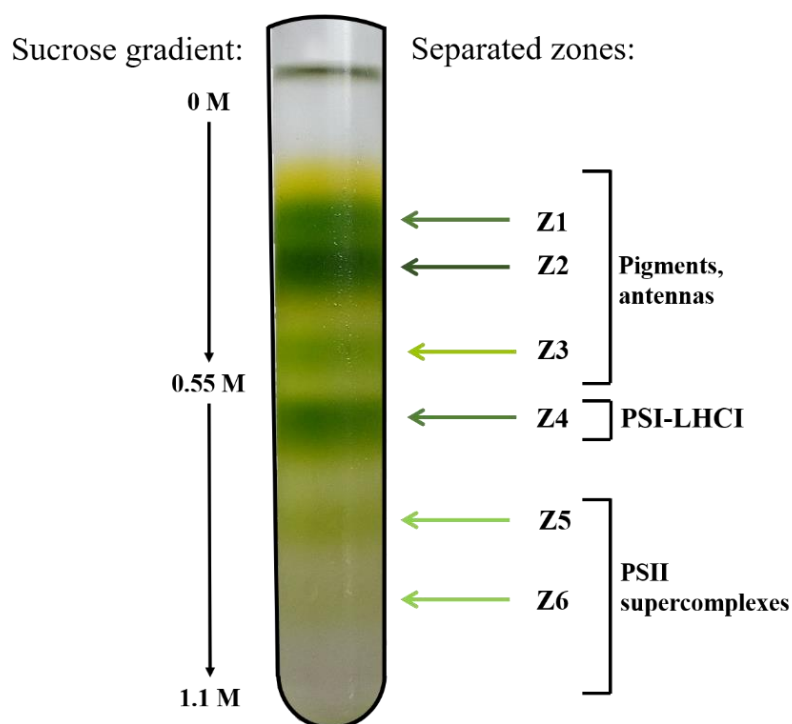

Figure 13. A centrifuge tube with photosynthetic thylakoid-membrane protein complexes separated in a continuous sucrose gradient into six zones Z1-Z6 and their assumed identification.

The individual zones were further examined by the 77K fluorescence emission spectroscopy and SDS-PAGE electrophoresis (see **Section 4**). The emission spectra of the six zones measured with 435 nm excitation wavelength are in **Fig. 14**. The significant peak at ~ 735 nm present almost solely in the Z4 spectrum confirmed the presence of PSI-LHCI in this zone, which is in accordance with previous research.[96] The maximum intensity

wavelengths of the other five zones varied from 680 to 690 nm. These zones presumably contain PSII and antenna complexes, single antennas, or pigments. However, further identification of these zones was not included in this study.

The electrophoretic gel with separated solubilized proteins of all zones is in **Fig 15a**. The different molecular masses of protein subunits visualized in a Coomassie blue stained gel highlighted the differences between the individual zones. A closer examination of the Z4 fraction can be seen in **Fig. 15b**. PsaA and PsaB, the largest PSI subunits, were identified in this zone according to previous studies.[98,99] Other lighter individual PSI and LHCI subunits are visible in the lower part of the gel.

Together, the fluorescence and electrophoretic analyses identified Z4 as the fraction with purified PSI-LHCI macromolecules.
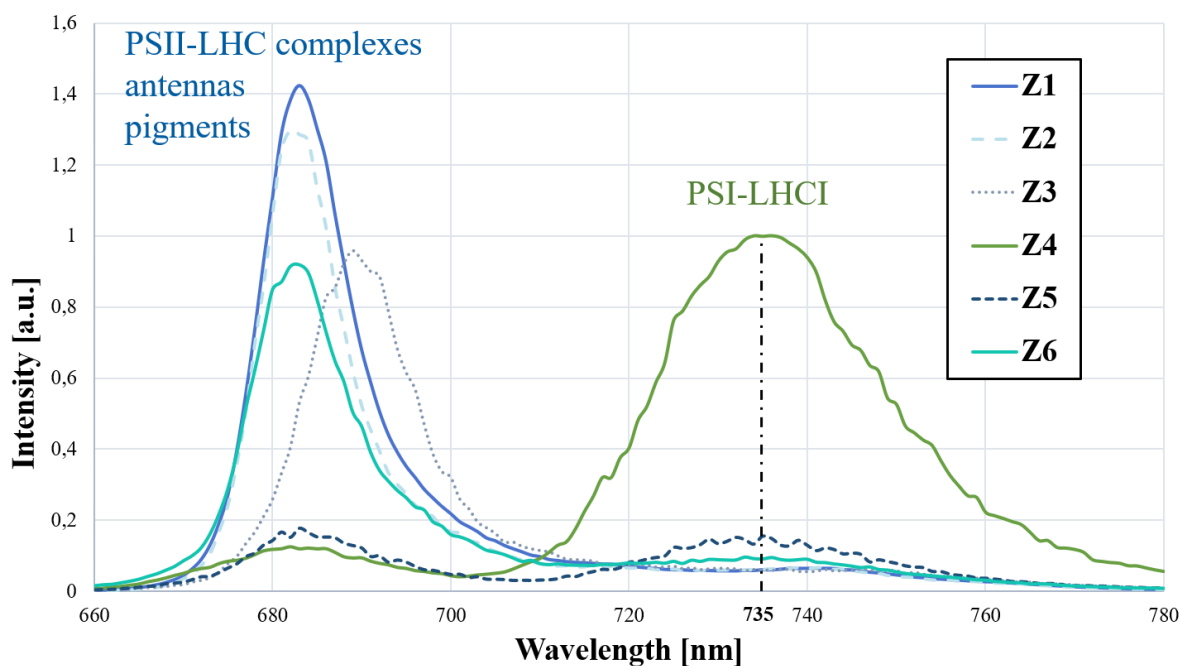

Figure 14. Fluorescence emission spectra of the Z1-Z6 zones previously separated by the continuous sucrose gradient, Z4 with the maximum intensity at ~ 735 nm containing PSI-LHCI complexes; the spectra were measured at 77 K and 435 nm excitation wavelength.
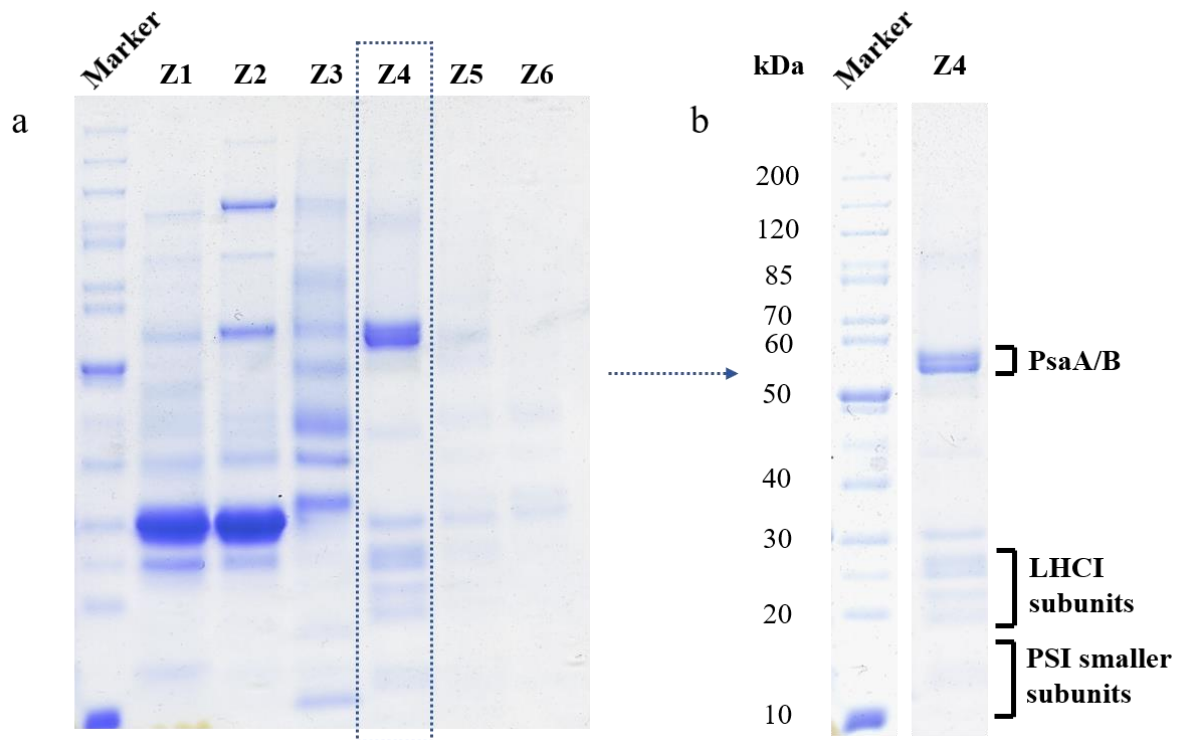
Figure 15. SDS-PAGE electrophoresis of the solubilized Z1-Z6 zones previously separated in the continuous sucrose gradient (gels stained in Coomassie blue): a) the electrophoretic gel with separated protein subunits of all zones and a marker, b) a comparison of the Z4 (PSI-LHCI) zone gel separation with the 10-200 kDa protein marker (PageRuler Unstained Protein Ladder); the two main PSI subunits (PsaA and PsaB) and other LHCI and PSI subunits are marked.

5.2 Microscopy visualization

Images of the negatively stained PSI-LHCI complexes were acquired by TEM at 20,000x magnification with 3.4 nm pixelsize (see **Section 4**). Approximately 100 micrographs were collected for each sample. Firstly, samples negatively stained by 2% aq. solutions of the evaluated salts were imaged. According to a standard UA staining procedure, all grids were prepared at once in advance to avoid the degradation of the freshly isolated PSI-LHCI complexes in a solution. The micrographs were then acquired with a >24 h delay from the preparation due to a high time consumption of the visualizing process. The time interval from the sample preparation to the imaging did not exceeded 5 days. Unexpectedly, the alternatively stained macromolecules exhibited a considerable decrease in the image quality in comparison to the UA stained sample. As a consequence, the particles prepared with SmN, EuN, GdN and HfC stains had to be picked manually for the further single particles analysis. Examples of unprocessed micrographs of each stain from the first set of visualization are in **Fig. 16**.
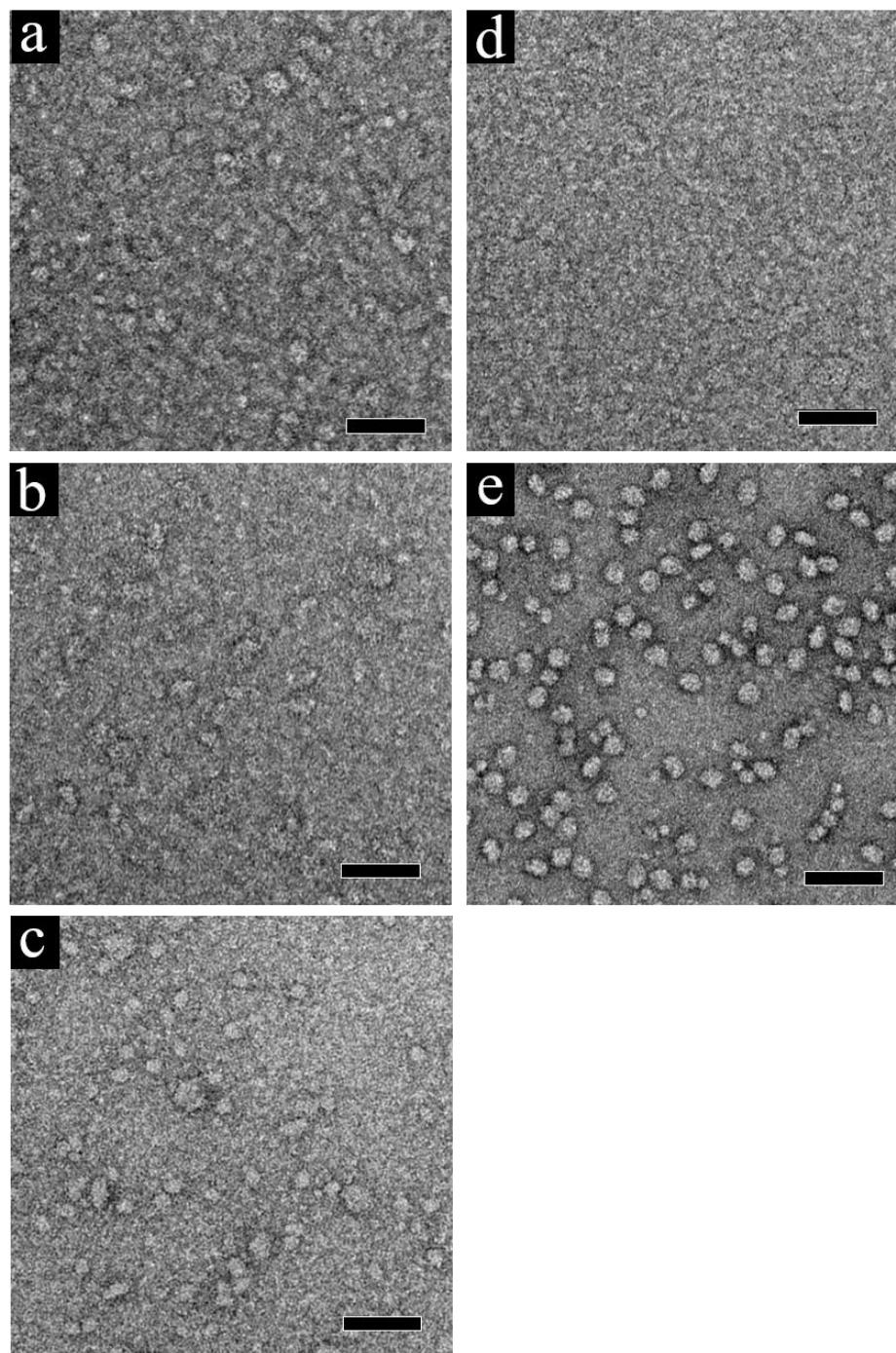
Figure 16. Examples of unprocessed images of the PSI-LHCI single macromolecules acquired by TEM with a >24h time delay between the sample preparation and the visualization, negatively stained with 2% w/w aq solutions of: a) EuN, b) GdN, c) HfC, d) SmN and e) UA; scalebar = 50 nm.

The alternatively stained samples were imaged again in the second set of visualizations. The sample preparation protocol was modified to lower the time delay to <24 h. A new PSI-LHCI isolation was performed before each day of microscoping, i.e. before the visualization of two differently stained samples in maximum. This approach, although more time-demanding, precluded the time degradation of both the isolated

macromolecules and the applied negative stains. The resulting image quality enabled an auto-picking of the particles for further analysis. Examples of unprocessed micrographs of each alternative stain from the second set of visualization with a comparison to the UA-stained sample from the first set are in **Fig. 17**.
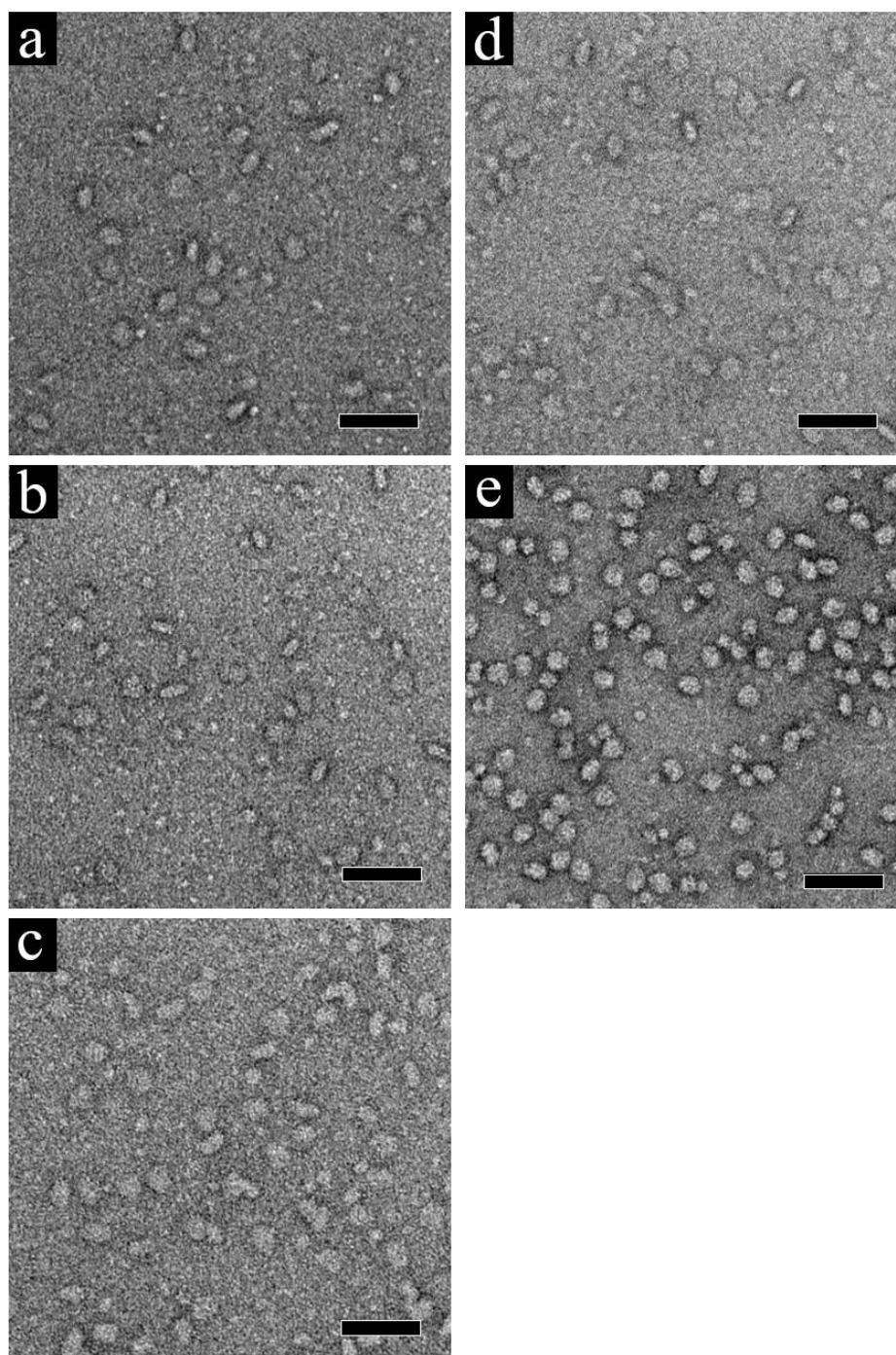

Figure 17. Examples of unprocessed images of the PSI-LHCI single macromolecules acquired by TEM with a <24h time delay between the sample preparation and the visualization (except for the UA), negatively stained with 2% w/w aq solutions of: a) EuN, b) GdN, c) HfC, d) SmN; e) UA (from the previous set of imaging as a comparison); scalebar = 50 nm.

The third set of micrographs was acquired to evaluate the potential influence of a stain concentration on the result. SmN was chosen from the list of the alternative stains due to its previous auspicious staining performance. New samples were stained by 1% and 3% w/w aq. SmN solutions, following the <24h protocol. Examples of unprocessed micrographs of each concentration level is in **Fig. 18**.
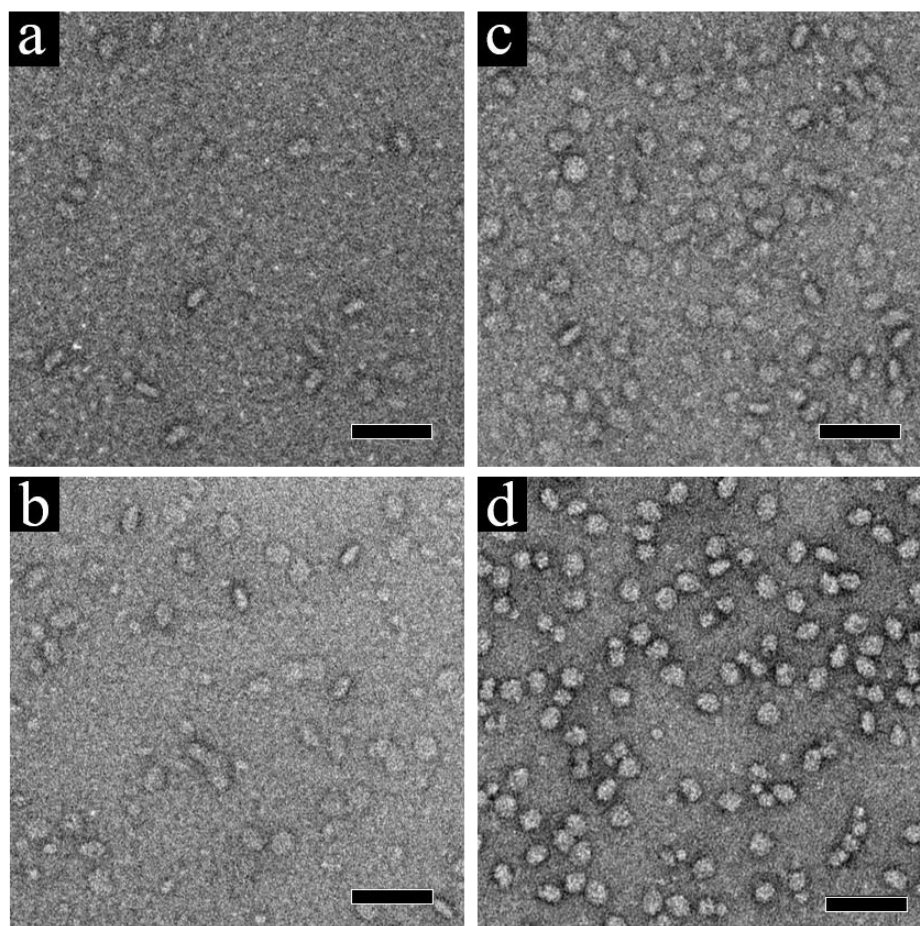

Figure 18. Examples of unprocessed images of the PSI-LHCI single macromolecules acquired by TEM with a <24h time delay between the sample preparation and the visualization, negatively stained with a) $SmN_{1\%}$ solution, b) $SmN_{2\%}$ solution (from the second set of imaging), c) $SmN_{3\%}$ solution, d) UA (from the first set of imaging as a comparison); scalebar = 50 nm.

5.3 Single particle analysis

The acquired images were processed in RELION (see **Section 4**) to obtain the 2D structure classifications of the PSI-LHCI macromolecules and their resolution to compare the quality of the result. A single particle analysis of the UA-stained sample was completed to verify the used method. 33,103 particles were automatically picked from the acquired micrographs, aligned into 2D classes and iterated. The most representative class

being aligned from the largest set of particles (1,083 in the case of UA) was selected for further evaluation. The micrographs of alternatively stained samples from all sets of visualization were processed in an equal way. The selected representative classes for all samples are shown in **Fig. 19**, where the sum of picked particles and the number of particles aligned in the particular class are denoted for each sample. The numbers of aligned particles were considerably lower at the >24h delayed alternatively stained samples. Therefore, only the classes of their <24h versions were taken for further evaluation. The classes omitted from the further evaluation are framed red in **Fig. 19**.
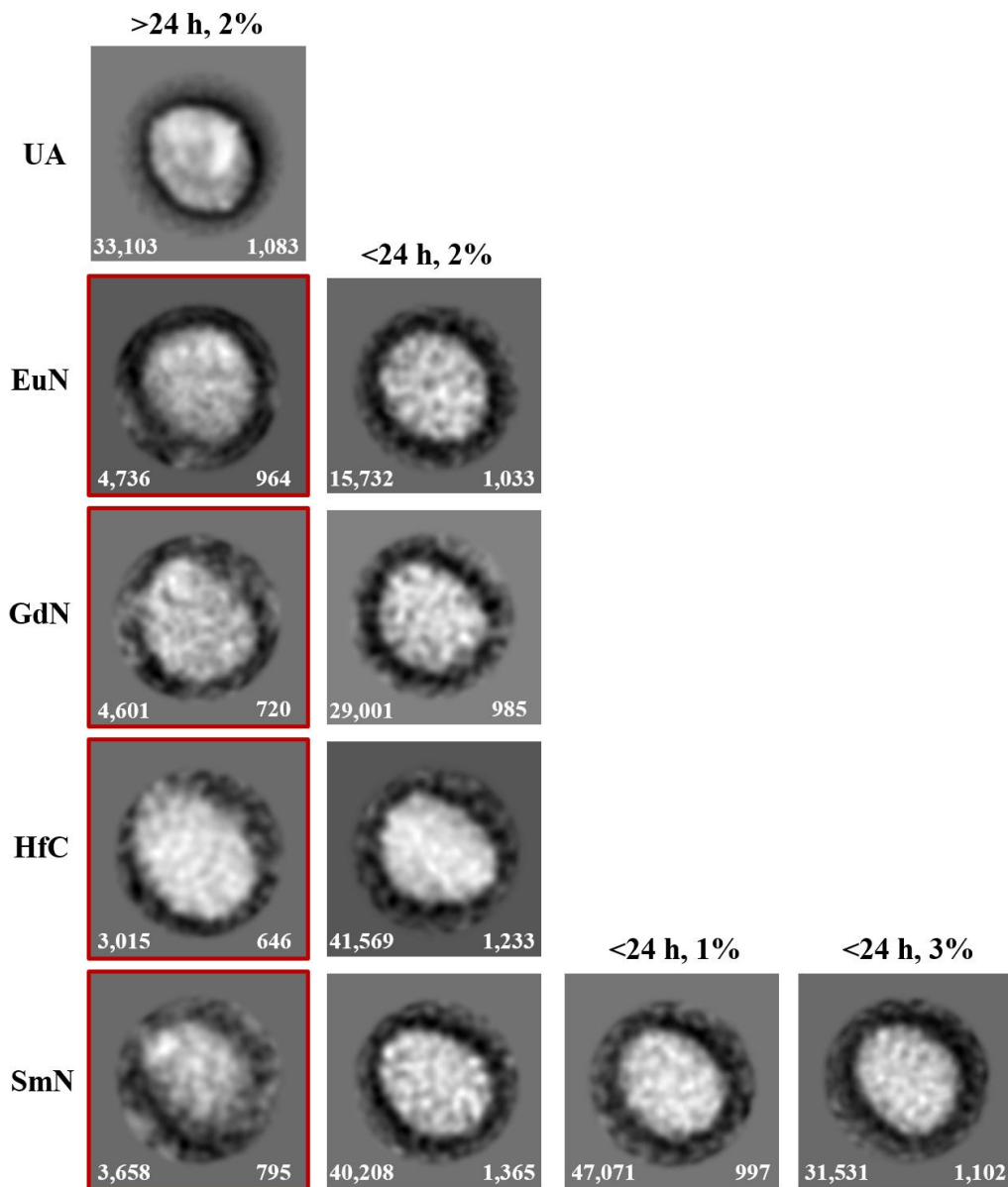

Figure 19. The representative classes obtained from the single particle analysis of each of the visualized sample; the sum of analyzed particles for each sample is in the lower-left corner, the number of particles aligned in the particular representative class is in the lower-right corner of each picture; the classes omitted from further evaluation due to the low number of aligned particles are framed red.

36

Firstly, the classes were evaluated based on their derived resolutions. The final resolution is to some extent dependent on the number of aligned particles (see **Section 4**). It is impossible to reach the same number of aligned particles per class that would be ideal for comparison with the used method. Thus, we present the derived resolutions of the representative classes together with the numbers of aligned particles in **Fig. 20**. The number of aligned particles varied from 985 (GdN) to 1,365 (SmN$_{2\%}$). No significant trend in the obtained resolutions was observed according to the numbers of particles. Thus, we further consider the variations in the numbers of particles as insignificant for the further resolution evaluation.
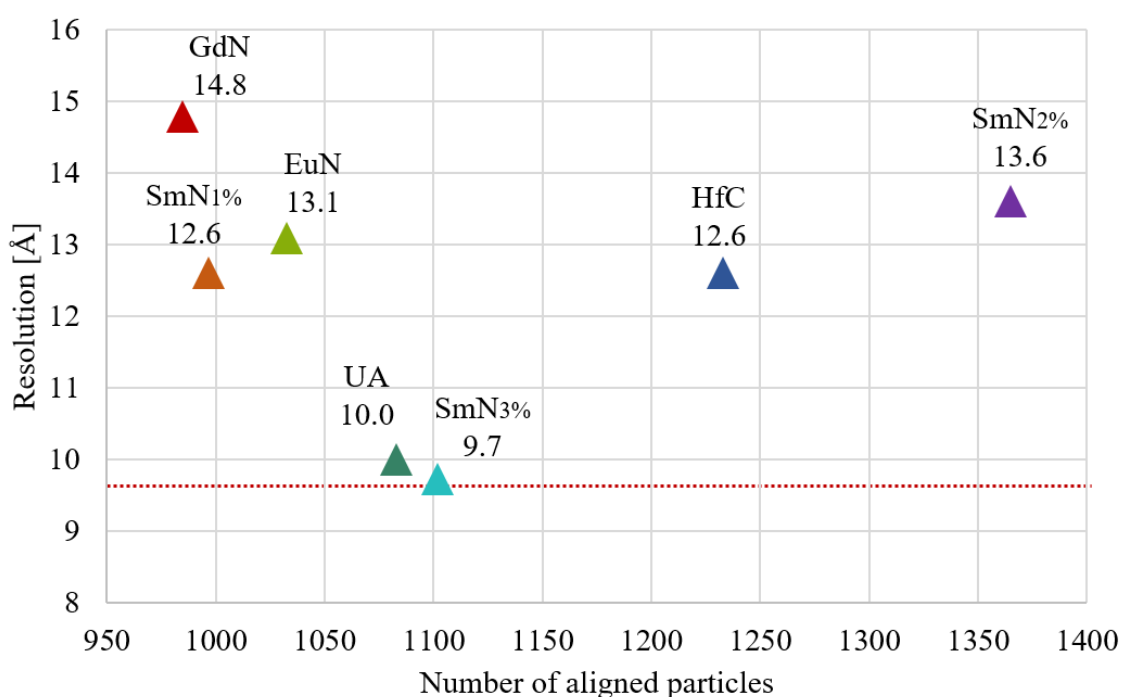

Figure 20. The derived values of resolution and the numbers of aligned particles for the representative classes of each of the alternatively stained samples with <24h time delay plus the UA-stained sample; red dashed line shows the lowest reached resolution (9.7 Å, SmN$_{3\%}$).

The highest resolution was obtained for the SmN$_{3\%}$-stained sample ($R_{SmN3\%}$ = 9.7 Å), the lowest for the 2% GdN-stained sample ($R_{GdN2\%}$ = 14.8 Å). The alternatively stained samples, except for the 3% Sm, did not reach a better resolution than the referential UA-stained sample ($R_{UA2\%}$ = 10.0 Å). No clear relation between the staining solution concentration and the resolution was observed at the SmN-stained samples ($R_{Sm1\%}$ = 12.6 Å, $R_{Sm2\%}$ = 13.6 Å, $R_{Sm3\%}$ = 9.7 Å). However, the resolution of the SmN$_{3\%}$ stain slightly surpassing that of UA is a promising result.

Even though the SmN$_{3\%}$ resolution could imply the stain usability, the single value of resolution is not capable of determining the potential of the negative stain to reveal the real structure. We further compared the obtained classes of the alternatively stained samples to the UA-stained sample in order to evaluate the reliability of the structural information. For this purpose, greyscale profiles were constructed for each of the representative classes (see **Section 4**). The direction and length for the grayscale profile construction of each particle was chosen as the shortest diameter of the oval-shaped PSI-LHCI particle. Firstly, the information yielded by the profile of UA-stained sample was compared with the real PSI-LHCI structure. The comparison is visualized in **Fig. 21**. The grayscale profiles of the other particles with denoted lines of which the profiles were constructed are in **Fig. 22**.
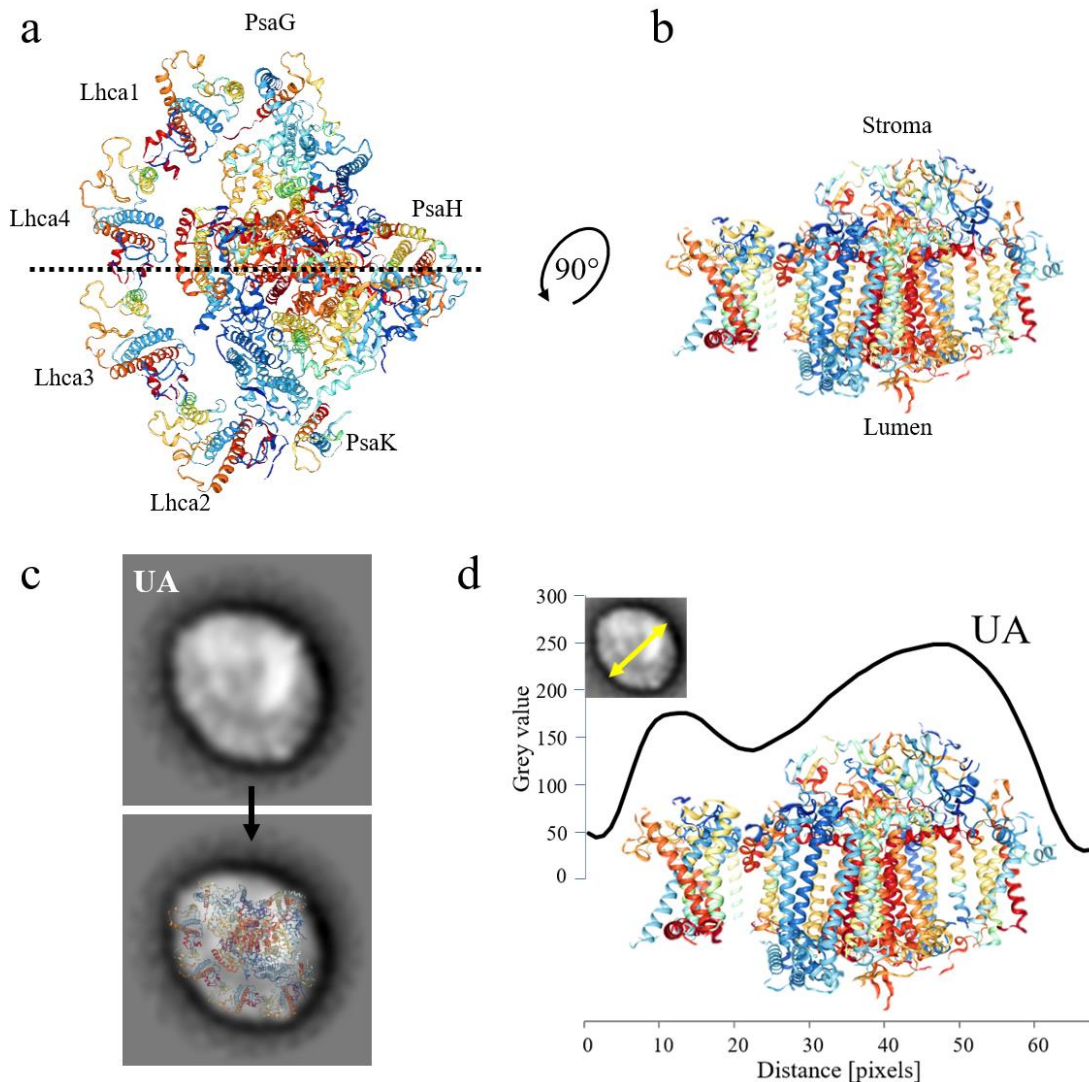
Figure 21. a) A stromal view on the 3D structure of plant PSI-LHCI complex at 2.6 Å resolution [71,100], b) a side view of the same structure rotated by 90° and cut according to the axis denoted in a); c) the representative class of the UA-stained sample with visible structural elements copying the real PSI-LHCI structure, d) the greyscale profile of the UA-stained sample with denoted line of the profile construction and with a side view of the PSI-LHCI structure in matching scale placed under the profile.

There are elements visible in the UA class that can be identified with the structural elements of the macromolecule (**Fig. 21c**), e.g. the LHCI subunits surrounding the PSI core or the specifically shaped subunits of the reaction centre. The side-view profile of the molecule X-ray model also consistently matches the greyscale profile of the imaged one (**Fig. 21d**), presuming a layer of the negative stain covering the structure. Both, the resemblance of the stromal view of the real structure and the representative class image (**Fig. 21c**) and the profile of the structure side view fitting under the greyscale profile of the class (**Fig. 21d**), confirm the reliability of the UA negative staining technique. The ability of the other negative stains to produce reliable information about the structure was therefore evaluated by comparing greyscale profiles (**Fig. 22**) to that of UA (**Fig. 21d**).
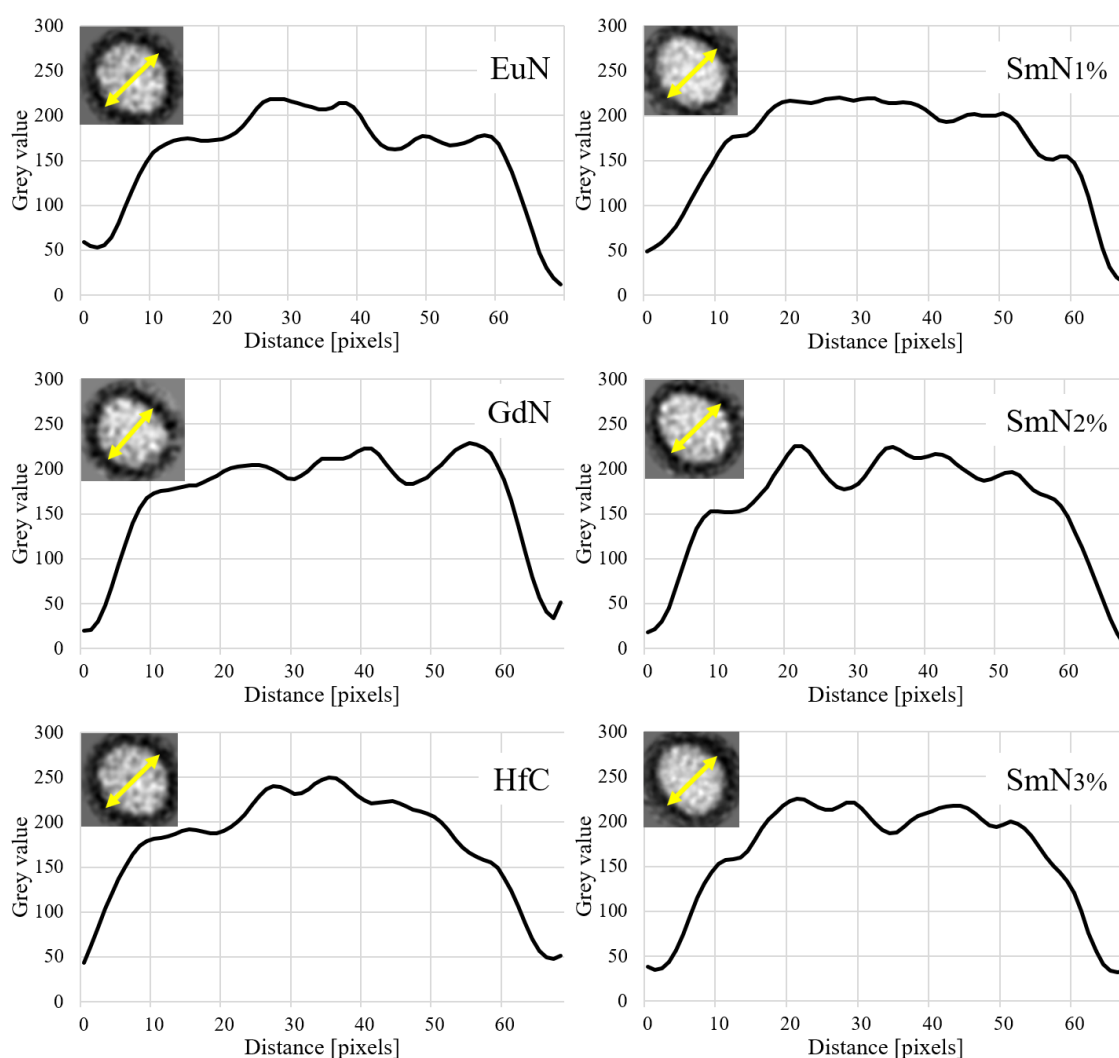

Figure 22. The grey-scale profiles of the representative classes of the alternatively stained particles with denoted lines from which they were constructed.

None of the greyscale profiles of the alternatively stained particles is similar to the profile of UA (**Fig. 21d**). The profiles generally consist of more peaks with little difference between them. Contrarily, the UA profile is clear with two significant peaks, one of them dominant. The profile of the before promising $SmN_{3\%}$-stained sample shows no difference from the other alternatively stained samples. According to the greyscale profile evaluation, the obtained 2D classified images of the alternatively stained particles could not be further used for a 3D structure determination or would probably yield misleading results. The possible explanation of these result is discussed below (see **Section 6**).

6 DISCUSSION

During the sample preparation, a considerably quick degradation of the alternatively stained samples was observed. This is in the contrast to the UA-stained samples, that are stable for a time sufficient to visualize several of them in equal quality (in the scale of days). Therefore, a certain fixative character of the UA stain is probably not present at the evaluated stains. The process of negative staining became several times more time demanding due to the necessity of fresh sample isolation and stain application before each visualization. One of the advantages of the standard EM negative staining technique would thus be eliminated using the alternative stains.

Another staining procedure-related observation was made with the HfC stain ($HfCl_4$). Unlike the other agents, this stain degraded even in the form of a solution (2% w/w aq.) and yielded images of significantly lower quality when applied after a week of storage. This phenomenon has been described before.[52] The HfC stain has to be prepared fresh before each staining which makes it slightly less convenient than the UA and lanthanide stains.

We compared the staining agents based on the obtained 2D maps resolution from the single particle analysis. The resolution of the UA-stained sample (10.0 Å) corresponds with the values generally obtainable by this method.[19] This result confirms the reliability of the performed staining technique. The theoretical resolution limit of negatively stained particles is not clearly described. It is to some extent based on the grain parameters of the staining molecule and on the process of the image digitalization, they are probably not the only attributes though. The previously widely recognized limit of 20-25 Å [101] has been credibly surpassed.[19] The now-prevailing theory puts the standard negative stain limit resolution below 10 Å.[19]

To date, the theoretical limit resolutions of the hafnium and lanthanide stains are not known. No accessible experiments with these stains were carried out on single particles so far. Therefore, $SmN_{3\%}$ reaching the resolution of 9.7 Å in our study is a very promising result. It implies a possible finer granularity of this stain compared to the UA. However, wider studies would have to be carried out to explain the result. The 9.7 Å resolution was reached with the 3% w/w aq. solution of the SmN stain. Thus, a more developed study of wider concentration range and perhaps different pH is necessary for the potential use of SmN as a negative stain.

The beforehand implied usability of the SmN stain is not aimed on the single particle EM, though. The second aspect of the evaluation revealed the inability of all the alternative stains

to yield a reliable structural information. Even though staining agents based on hafnium, samarium or gadolinium have proved to be applicable in equal quality to UA in the negative staining of ultrathin sections, virions, or fibrils [51,52,102], no previous research was made on the single macromolecules. In this study we propose such stains inapplicable for this purpose. The potential 3D reconstruction of the obtained 2D maps would result in a false structure. Unless research focused on the chemistry of the staining molecules is carried out, the explanation of such misleading results is not obtainable. We suggest a potential aggregation of the staining molecules or undesired reactions of them upon the contact with the stained macromolecule could be the cause of covering the macromolecule by not copying its surface exactly. An investigation of the stains' behaviour in different conditions, such as in other than aqueous solutions or in a different pH, would be beneficial for further use in the single particle EM.

7 CONCLUSION

The aim of this study was to test several new potential alternatives to uranyl acetate as a negative stain in single particle electron microscopy. The search for new staining reagents has been recently enhanced by increasing complications in the UA purchase derived from its chemical toxicity and radioactivity. Some of the tested chemicals already proved their usability. However, no accessible studies were performed on single particles.

We chose hafnium chloride and europium, samarium and gadolinium nitrates as the tested negative stains. None of these chemicals are considered as health-threatening and all of them are easy to purchase.

The stains were applied on a sample, visualized in a transmission electron microscope and classified by a single particle analysis into 2D electron maps. Plant photosystem I was selected as the sample macromolecule for its well described structure and a convenient isolation.

The quality of the staining properties was evaluated by two factors, the obtained resolution of the 2D class and the possibility to yield a reliable structural information. The results were compared with a referential UA-stained sample.

Firstly, we observed a promising result of the SmN stain resolution (9.7 Å) surpassing that of the UA (10.0 Å). Such phenomenon implied good staining properties of the SmN stain. However, these properties are not usable in the single particle electron microscopy as was revealed by the evaluation of the second factor. The greyscale profiles of the alternatively stained classified particles, in contrast to the UA-stained, did not correspond with the profile of the X-ray model of the macromolecule and further 3D reconstructions would yield false structures.

We suggest undesirable reactions of the stain molecules upon the contact with the macromolecular surface or their aggregation in a solution as possible causes of the obtained negative results. They would have to be proved by advanced research, though. A detailed study of the SmN staining properties in different conditions would be also beneficial to establish its usability as a negative stain at least in other fields of electron microscopy.

8 LIST OF REFERENCES

1. Frank, J. Advances in the field of single-particle cryo-electron microscopy over the last decade. *Nat. Protoc.* **12,** 209–212 (2017).

2. Alberts, B. *et al.* Analyzing Protein Structure and Function in *Molecular Biology of the Cell 4th edition.* (Garland Science, 2002).

3. Smyth, M. S. & Martin, J. H. X Ray Crystallography. *Mol. Pathol.* **53,** 8–14 (2000).

4. Picknett, T. M. & Brenner, S. X-Ray Crystallography in *Encyclopedia of Genetics* 2154 (Elsevier, 2001).

5. Rcsb.org. *PDB Data Distribution by Experimental Method and Molecular Type*. Available at: https://www.rcsb.org/stats/summary [Accessed 5 Feb. 2018].

6. Wiithrich, K. Protein Structure Determination in Solution by NMR Spectroscopy. *JOURNAL. Biol. Chem.* **265,** 22059–22062 (1990).

7. Berg, J. M., Tymoczko, J. L. & Stryer, L. Three-Dimensional Protein Structure Can Be Determined by NMR Spectroscopy and X-Ray Crystallography in *Biochemistry 5th edition.* (W H Freeman, 2002).

8. Kühlbrandt, W. Biochemistry. The resolution revolution. *Science* **343,** 1443–4 (2014).

9. Bai, X., McMullan, G. & Scheres, S. H. How cryo-EM is revolutionizing structural biology. *Trends Biochem. Sci.* **40,** 49–57 (2015).

10. Carroni, M. & Saibil, H. R. Cryo electron microscopy to determine the structure of macromolecular complexes. *Methods* **95,** 78–85 (2016).

11. Stark, H. & Chari, A. Sample preparation of biological macromolecular assemblies for the determination of high-resolution structures by cryo-electron microscopy. *Microscopy* **65,** 23–34 (2016).

12. Bozzola, J. J. and Russell, L.D. *Electron Microscopy, Second Edition.* (Jones and Bartlett Publishers, Inc., 1999).

13. Williams, D. and Carter, B. *Transmission electron microscopy*. (Springer, 2009).

14. Murphy, D. B. *Fundamentals of light microscopy and electronic imaging*. (Wiley-Liss, 2001).

15. Haider, M. *et al.* A spherical-aberration-corrected 200 kV transmission electron microscope. *Ultramicroscopy* **75,** 53–60 (1998).

16. Smith, D. J. Ultimate resolution in the electron microscope? *Mater. Today* **11,** 30–38 (2008).

17. Urban, K. W. Studying atomic structures by aberration-corrected transmission electron microscopy. *Science* **321,** 506–10 (2008).

18. JEOL, Ltd. *Introduction to JEOL Products*. Available at: www.jeol.co.jp [Accessed 13 Mar. 2018].

19. Boekema, E. J., Folea, M. & Kouřil, R. Single particle electron microscopy. *Photosynth. Res.* **102,** 189–96 (2009).

20. Hite, R. K., Raunser, S. & Walz, T. Revival of electron crystallography. *Curr. Opin. Struct. Biol.* **17,** 389–95 (2007).

21. Kühlbrandt, W., Wang, D. N. & Fujiyoshi, Y. Atomic model of plant light-harvesting complex by electron crystallography. *Nature* **367,** 614–621 (1994).

22. De Carlo, S. & Robin Harris, J. Negative staining and Cryo-negative Staining of Macromolecules and Viruses for TEM. *Micron*, **42(2)**, 117-131 (2011)

23. Zobel, C. R. & Roe, J.-Y. K. Positive staining of protein molecules for electron microscopy. *Biochim. Biophys. Acta - Protein Struct.* **133,** 157–161 (1967).

24. Thompson, R. F., Walker, M., Siebert, C. A. & Ranson, N. A. An introduction to sample preparation and imaging by cryo-electron microscopy for structural biology. *Methods* **100,** 3–15 (2016).

25. Advanced Chemistry Development, Inc., Toronto, ON, Canada. ACD/ChemSketch (Freeware), version 12.01,. Available at: www.acdlabs.com (2010).

26. Klaproth, M. H. Chemische Untersuchung des Uranits, einer neuentdeckten metallischen Substanz. *Chemische Annalen.* **2**: 387–403 (1789).

27. *Péligot, E.-M.* Recherches Sur L'Uranium. *Annales de chimie et de physique. 5 (5): 5-47 (1842).*

28. Emsley, J. *Nature's building blocks : an A-Z guide to the elements*. (Oxford University Press, 2001).

29. Yazzie, M., Gamble, S., Civitello, E. and Stearns, D. Uranyl Acetate Causes DNA Single Strand Breaks In Vitro in the Presence of Ascorbate (Vitamin C). *Chemical Research in Toxicology*, **16(4)**, 524-530 (2003).

30. Ronen, Y. Some remarks on the fissile isotopes. *Ann. Nucl. Energy* **37,** 1783–1784 (2010).

31. Stearns, D. M. *et al.* Uranyl acetate induces hprt mutations and uranium–DNA adducts in Chinese hamster ovary EM9 cells. *Mutagenesis* **20,** 417–423 (2005).

32. Priest, N. Toxicity of depleted uranium. *Lancet* **357,** 244–246 (2001).

33. Durakovic, A. Medical effects of internal contamination with actinides: further controversy on depleted uranium and radioactive warfare. *Environ. Health Prev. Med.* **21,** 111–7 (2016).

34. Conklin, J. *Military Radiobiology.* (Elsevier Science, 1987).

35. Mulloy, K. B., James, D. S., Mohs, K. & Kornfeld, M. Lung cancer in a nonsmoking underground uranium miner. *Environ. Health Perspect.* **109,** 305–9 (2001).

36. Kryscio, A. *et al.* A cytogenetic analysis of the long-term effect of uranium mining on peripheral lymphocytes using the micronucleus–centromere assay. *Int. J. Radiat. Biol.* **77,** 1087–1093 (2001).

37. Ozmen, M. & Yurekli, M. Subacute toxicity of uranyl acetate in Swiss-Albino mice. *Environ. Toxicol. Pharmacol.* **6,** 111–115 (1998).

38. Mahmood, I. & Waters, D. H. A comparative study of uranyl nitrate and-cisplatin-induced renal failure in rat. *Eur. J. Drug Metab. Pharmacokinet.* **19,** 327-36 (1994)

39. Domingo, J. L., Llobet, J. M., Tomás, J. M. & Corbella, J. Acute toxicity of uranium in rats and mice. *Bull. Environ. Contam. Toxicol.* **39,** 168–74 (1987).

40. Bentley, K. W., Stockwell, D. R., Britt, K. A. & Kerr, C. B. Transient proteinuria and aminoaciduria in rodents following uranium intoxication. *Bull. Environ. Contam. Toxicol.* **34,** 407–16 (1985).

41. Anthony, M. L., Gartland, K. P., Beddell, C. R., Lindon, J. C. & Nicholson, J. K. Studies of the biochemical toxicology of uranyl nitrate in the rat. *Arch. Toxicol.* **68,** 43-53 (1994).

42. Khan, M. M. T. & Martell, A. E. Kinetics of metal ion and metal chelate catalyzed oxidation of ascorbic acid. IV. Uranyl ion catalyzed oxidation. *J. Am. Chem. Soc.* **91,** 4668–4672 (1969).

43. Hamilton, M., Ejnik, J. and Carmichael, A. Uranium reactions with hydrogen peroxide studied by EPR–spin trapping with DMPO†. *Journal of the Chemical Society, Perkin Transactions 2*. **12**, 2491-2494 (1997).

44. Miller, A. C., Stewart, M., Brooks, K., Shi, L. & Page, N. Depleted uranium-catalyzed oxidative DNA damage: absence of significant alpha particle decay. *J. Inorg. Biochem.* **91,** 246–52 (2002).

45. Keith S, Faroon O, Roney N, et al. Toxicological Profile for Uranium. Atlanta (GA): Agency for Toxic Substances and Disease Registry (US). (2013) Available from: https://www.ncbi.nlm.nih.gov/books/NBK158805/table/T15/

46. American Conference of Governmental Industrial Hygienists TLVs and BEIs. Threshold Limit Values for Chemical Substances and Physical Agents and Biological Exposure Indices. Cincinnati, OH, 2008, p. 59

47. Hosogi, N., Nishioka, H. & Nakakoshi, M. Evaluation of lanthanide salts as alternative stains to uranyl acetate. *Microscopy* **64,** 429–435 (2015).

48. Sato, S., Adachi, A., Sasaki, Y. & Ghazizadeh, M. Oolong tea extract as a substitute for uranyl acetate in staining of ultrathin sections. *J. Microsc.* **229,** 17–20 (2008).

49. Inaga, S. *et al.* Platinum blue as an alternative to uranyl acetate for staining in transmission electron microscopy. *Arch. Histol. Cytol.* **70,** 43–49 (2007).

50. Yamaguchi, K., Suzuki, K. i. & Tanaka, K. Examination of electron stains as a substitute for uranyl acetate for the ultrathin sections of bacterial cells. *J. Electron Microsc. (Tokyo).* **59,** 113–118 (2010).

51. Nakakoshi, M., Nishioka, H. & Katayama, E. New versatile staining reagents for biological transmission electron microscopy that substitute for uranyl acetate. *J. Electron Microsc. (Tokyo).* **60,** 401–407 (2011).

52. Ikeda, K.-I., Inoue, K., Kanematsu, S., Horiuchi, Y. & Park, P. Enhanced effects of nonisotopic hafnium chloride in methanol as a substitute for uranyl acetate in TEM contrast of ultrastructure of fungal and plant cells. *Microsc. Res. Tech.* **74,** n/a-n/a (2010).

53. Kim, S. et al. PubChem Substance and Compound databases. *Nucleic Acids Research* 44, D1202-D1213 (2015).

54. Edelstein, N. M.. *Lanthanide and Actinide Chemistry and Spectroscopy*. (American Chemical Society, 1980).

55. D'Angelo, P. *et al.* Revised Ionic Radii of Lanthanoid(III) Ions in Aqueous Solution. *Inorg. Chem.* **50,** 4572–4579 (2011).

56. Bünzli, J.-C., G. Lanthanides in *Encyclopedia of Chemical Technology.* (Wiley Blackwell, 2013).

57. Kilbourn, B. T. The role of the lanthanides in applied catalysis. *J. Less Common Met.* **126,** 101–106 (1986).

58. Selvin, P. R. Principles and Biophysical Applications of Lanthanide-Based Probes. *Annu. Rev. Biophys. Biomol. Struct* **31,** 275–302 (2002).

59. Palizban, A. A., Sadeghi-Aliabadi, H. & Abdollahpour, F. Effect of cerium lanthanide on Hela and MCF-7 cancer cell growth in the presence of transferring. *Res. Pharm. Sci.* **5,** 119–25 (2010).

60. Audi, G., Bersillon, O., Blachot, J. & Wapstra, A. H. The NUBASE evaluation of nuclear and decay properties. *Nuclear Physics A* 729, 3-128 (2003).

61. ECHA, European chemicals agency, Available at: www.echa.europa.eu [Accessed 19 Feb. 2018]

62. Hafnium | chemical element. *Encyclopedia Britannica*. Avaliable at www.britannica.com/science/hafnium [Accessed 12 Feb. 2018]

63. Hynninen, P. H., Leppäkases, T. S. The Function of Chlorophylls in Photosynthesis in *Physiology and Maintenance, Volume V*, (Eolss Publishers, 2009)

64. Nelson, N. & Ben-Shem, A. The complex architecture of oxygenic photosynthesis. *Nat. Rev. Mol. Cell Biol.* **5,** 971–982 (2004).

65. Nelson, N. & Ben-Shem, A. The structure of photosystem I and evolution of photosynthesis. *BioEssays* **27,** 914–922 (2005).

66. Allen, J. F., de Paula, W. B. M., Puthiyaveetil, S. & Nield, J. A structural phylogenetic map for chloroplast photosynthesis. *Trends Plant Sci.* **16,** 645–655 (2011).

67. Amunts, A., Drory, O. & Nelson, N. The structure of a plant photosystem I supercomplex at 3.4 Å resolution. *Nature* **447,** 58–63 (2007).

68. DuysenS, L. N. M., Amesz, J. & Kamp, B. M. Two Photochemical Systems in Photosynthesis. *Nature* **190,** 510–511 (1961).

69. Fromme, P. & Mathis, P. Unraveling the Photosystem I Reaction Center: A History, or the Sum of Many Efforts. *Photosynth. Res.* **80,** 109–124 (2004).

70. Ben-Shem, A., Frolow, F. & Nelson, N. Crystal structure of plant photosystem I. *Nature* **426,** 630–635 (2003).

71. Mazor, Y., Borovikova, A., Caspy, I. & Nelson, N. Structure of the plant photosystem i supercomplex at 2.6 Å resolution. *Nat. Plants* **3,** 1–9 (2017).

72. Boekema, E. J., Wynn, R. M. & Malkin, R. The structure of spinach Photosystem I studied by electron microscopy. *Biochim. Biophys. Acta - Bioenerg.* **1017,** 49–56 (1990).

73. Boekema, E. J., Boonstra, A. F., Dekker, J. P. & R�gner, M. Electron microscopic structural analysis of Photosystem I, Photosystem II, and the cytochromeb6/f complex from green plants and cyanobacteria. *J. Bioenerg. Biomembr.* **26,** 17–29 (1994).

74. Gardian, Z., Tichý, J. & Vácha, F. Structure of PSI, PSII and antennae complexes from yellow-green alga Xanthonema debile. *Photosynth. Res.* **108,** 25–32 (2011).

75. Bína, D., Gardian, Z., Vácha, F. & Litvín, R. Supramolecular organization of photosynthetic membrane proteins in the chlorosome-containing bacterium Chloroflexus aurantiacus. *Photosynth. Res.* **122,** 13–21 (2014).

76. Sigma-Aldrich, *n*-Dodecyl β-D-maltoside, Available at: www.sigmaaldrich.com/catalog/product/sigma, [Accessed 10 Mar. 2018]

77. Raschke, S., Guan, J. & Iliakis, G. in *Methods in molecular biology (Clifton, N.J.)* **521,** 329–342 (2009).

78. D'Amici, G. M., Huber, C. G. & Zolla, L. in *Methods in molecular biology (Clifton, N.J.)* **528,** 60–70 (2009).

79. Chen, Y. E., Yuan, S. & Schröder, W. P. Comparison of methods for extracting thylakoid membranes of Arabidopsis plants. *Physiol. Plant.* **156,** 3–12 (2016).

80. Lamb, J., Forfang, K. & Hohmann-Marriott, M. A Practical Solution for 77 K Fluorescence Measurements Based on LED Excitation and CCD Array Detector. *PLoS One* **10,** e0132258 (2015).

81. Scheres, S. H. W. RELION: Implementation of a Bayesian approach to cryo-EM structure determination. *J. Struct. Biol.* **180,** 519–530 (2012).

82. Sigworth, F. J., Doerschuk, P. C., Carazo, J.-M. & Scheres, S. H. W. An introduction to maximum-likelihood methods in cryo-EM. *Methods Enzymol.* **482,** 263–94 (2010).

83. Carazo, J.-M. The Fidelity of 3D Reconstructions from Incomplete Data and the Use of Restoration Methods in *Electron Tomography* 117–164 (Springer US, 1992).

84. Scheres, S. H. W. & Chen, S. Prevention of overfitting in cryo-EM structure determination. *Nat. Methods* **9,** 853–4 (2012).

85. Chen, S. *et al.* High-resolution noise substitution to measure overfitting and validate resolution in 3D structure determination by single particle electron cryomicroscopy. *Ultramicroscopy* **135,** 24–35 (2013).

86. Penczek, P. A. Resolution measures in molecular electron microscopy. *Methods Enzymol.* **482,** 73–100 (2010).

87. Van Heel, M. Similarity measures between images. *Ultramicroscopy* **21,** 95–100 (1987).

88. Van Heel, M. & Schatz, M. Fourier shell correlation threshold criteria. *J. Struct. Biol.* **151,** 250–262 (2005).

89. Rosenthal, P. B. & Henderson, R. Optimal Determination of Particle Orientation, Absolute Hand, and Contrast Loss in Single-particle Electron Cryomicroscopy. *J. Mol. Biol.* **333,** 721–745 (2003).

90. Prasad, V. M. *et al.* Structure of the immature Zika virus at 9 Å resolution. *Nat. Struct. Mol. Biol.* **24,** 184–186 (2017).

91. Liao, H. Y. & Frank, J. Definition and estimation of resolution in single-particle reconstructions. *Structure* **18,** 768–75 (2010).

92. Wade, R. H. A brief look at imaging and contrast transfer. *Ultramicroscopy* **46,** 145-156 (1992).

93. Scheres, S. H. W. Single-particle processing in relion-2.1 (RELION tutorial), Available at: ftp://ftp.mrc-lmb.cam.ac.uk/pub/scheres/relion21_tutorial.pdf [Accessed 13 Mar. 2018]

94. Gardian, Z., Litvín, R., Bína, D. & Vácha, F. Supramolecular organization of fucoxanthin-chlorophyll proteins in centric and pennate diatoms. *Photosynth. Res.* **121,** 79–86 (2014).

95. *Schneider, C. A.; Rasband, W. S. & Eliceiri, K. W.* NIH Image to ImageJ: 25 years of image analysis*, Nature methods 9(7): 671-675, (2012)*

96. Galka, P. *et al.* Functional Analyses of the Plant Photosystem I-Light-Harvesting Complex II Supercomplex Reveal That Light-Harvesting Complex II Loosely Bound to Photosystem II Is a Very Efficient Antenna for Photosystem I in State II. *Plant Cell* **24,** 2963–2978 (2012).

97. Ballottari, M., Govoni, C., Caffarri, S. & Morosinotto, T. Stoichiometry of LHCI antenna polypeptides and characterization of gap and linker pigments in higher plants Photosystem I. *Eur. J. Biochem.* **271,** 4659–4665 (2004).

98. Scheller, H. V., Jensen, P. E., Haldrup, A., Lunde, C. & Knoetzel, J. Role of subunits in eukaryotic Photosystem I. *Biochim. Biophys. Acta - Bioenerg.* **1507,** 41–60 (2001).

99. Hu, Q. *et al.* A photosystem I reaction center driven by chlorophyll d in oxygenic photosynthesis. *Proc. Natl. Acad. Sci. U. S. A.* **95,** 13319–23 (1998).

100. Rose, A. S., Hildebrand, P. W. NGL Viewer: a web application for molecular visualization. *Nucl Acids Res* **43** (2015)

101. Ohi, M., Li, Y., Cheng, Y. & Walz, T. Negative Staining and Image Classification - Powerful Tools in Modern Electron Microscopy. *Biol. Proced. Online* **6,** 23–34 (2004).

102. Inoue, K., Muranaka, Y., Park, P. & Yasuda, H. Exploration of non-radioactive alternative stains to uranyl acetate in *European Microscopy Congress 2016: Proceedings* 461–462 (Wiley-VCH Verlag GmbH & Co. KGaA, 2016).